Recovery of a learned behavior despite partial restoration of neuronal dynamics after chronic inactivation of inhibitory neurons

Zsofia Torok[1]*, *Laura Luebbert*[1], *Jordan Feldman*[1], *Alison Duffy*[3], *Alexander A. Nevue*[4], *Shelyn Wongso*[1], *Claudio V. Mello*[4]‡, *Adrienne Fairhall*[3]‡, *Lior Pachter*[1,2]‡, *Walter G. Gonzalez*[5]‡, *Carlos Lois*[1]*‡

[1]Division of Biology and Biological Engineering, California Institute of Technology; Pasadena, CA, USA.
[2]Department of Computing and Mathematical Sciences, California Institute of Technology; Pasadena, CA, USA.
[3]University of Washington; Seattle, WA, USA.
[4]Oregon Health & Science University; Portland, OR, USA.
[5]Department of Physiology, University of San Francisco; San Francisco, CA, USA.
‡Senior authors
*Corresponding authors. Email: clois@caltech.edu (C.L.); zsofia.torok@ucsf.edu (Z.T.)

Abstract

Maintaining motor skills is crucial for an animal's survival, enabling it to endure diverse perturbations throughout its lifespan, such as those caused by trauma, disease, and aging. What mechanisms orchestrate brain circuit reorganization and recovery to preserve the stability of behavior despite the prolonged presence of a disturbance? To investigate this question, we chronically silenced a significant fraction of inhibitory neurons in a brain nucleus necessary for singing in zebra finches. Song in zebra finches is a complex, learned motor behavior. This manipulation altered brain activity and severely perturbed song; however, the behavior was precisely restored two months later. Single-cell RNA sequencing revealed that chronic silencing of interneurons led to elevated numbers of microglia and increased expression of MHC I, which were also observed in normal juveniles during song learning. Electrophysiology recordings revealed abnormal offline dynamics, some aspects of which returned to normal as the song recovered. However, even after the song had fully recovered, the levels of neuronal firing in premotor and motor areas involved in song production did not return to normal levels. These experiments demonstrate that the adult brain can overcome extended periods of abnormal activity and precisely restore a complex behavior without recovering the original neuronal dynamics.

Introduction

For most animals, precisely executing behaviors throughout life, despite perturbations due to trauma, disease, or aging, is crucial for reproduction and survival. To reliably perform behaviors, brain circuits require a balance of excitation and inhibition (E/I balance) to maintain physiological activity patterns. Loss of E/I balance causes abnormal patterns of neuronal activity, which can result in diseases such as epilepsy [1,2]. Given its importance, brain circuits strive to restore E/I balance once disturbed [3]. However, the characteristics of circuit reorganization and recovery of E/I balance after extensive and long-term perturbation remain poorly understood.

Zebra finches produce a highly stereotyped song with minimal variability over extended periods of time [4], underpinned by temporally precise neural activity [5]. This species thus provides an ideal model to monitor how abnormal brain activity affects behavior over time. Here, we genetically blocked

inhibitory neurons in HVC (proper name), a premotor brain nucleus of the male zebra finch involved in song production, to chronically perturb the E/I balance. HVC contains two main types of excitatory neurons that project to two main downstream targets: nucleus X (proper name) and nucleus RA (robust nucleus of the arcopallium). In addition, HVC includes several types of inhibitory neurons whose axons do not leave HVC; thus, they act locally within HVC [5]. Previous work has shown that acutely blocking interneuron signaling in adult finches by chemicals perturbs behavior for a few hours until the chemical is washed out, after which normal behavior is restored [6]. However, these acute, transient perturbations offer limited insight into the mechanisms by which brain circuits can recover normal function and restore behavior for extended periods. Thus, the long-term impact of chronic muting of interneurons on neuronal dynamics and the potential for behavior and brain state recovery after these perturbations remain unexplored. To investigate this question, we chronically silenced a large fraction of inhibitory neurons in the HVC of adult zebra finches, which altered brain activity and severely perturbed their songs for around two months. Persistent suppression of interneuron activity resulted in increased numbers of microglia and transcription of the major histocompatibility complex class I (MHC I) gene during the peak of behavioral distortion, suggesting the potential involvement of inflammatory and immune signaling pathways in neural circuit reorganization.

Interestingly, microglia levels reverted to baseline upon the onset of behavioral recovery. Electrophysiology recordings revealed that song degradation was paralleled by abnormal offline activity in HVC; however, subsequent recovery of the behavior occurred despite incomplete normalization of HVC activity. These experiments demonstrate that the adult brain can recover after extended periods of drastic abnormal activity and reveal some of the cellular mechanisms that potentially mediate functional restoration after long-term perturbation. In addition, we demonstrate that the adult brain can precisely restore a complex behavior without recovering the original neuronal dynamics.

Results

Permanent genetic muting of inhibitory neurons in HVC leads to zebra finch song degradation and an increase in the number of microglia and expression of MHC class I genes

To investigate how a complex behavior responds to the chronic loss of inhibitory tone, we permanently blocked the function of HVC inhibitory neurons in adult male zebra finches by bilateral stereotaxic injection of an AAV viral vector into HVC. The AAV viral vector carried the light chain of tetanus toxin (TeNT), driven by the human dlx5 promoter, which is selectively active in inhibitory neurons[7]. TeNT blocks the release of neurotransmitters from presynaptic terminals, thereby preventing neurons from communicating with their postsynaptic partners [8]. Thus, the expression of TeNT does not directly alter the ability of neurons to fire action potentials but effectively mutes them. As a control, a second group of animals was injected with an AAV carrying the green fluorescent protein NeonGreen driven by the ubiquitous promoter CAG. Throughout various time points in this perturbation paradigm, we recorded songs, measured changes in gene expression at single-cell resolution, and obtained electrophysiological measurements (chronic and acute within HVC).

An average male zebra finch song contains 4 to 7 units called syllables. These syllables are fixed in order and make up a motif repeated multiple times to form a bout [9–11]. A bout defines the length of a

vocally active period in adult animals. Throughout all experiments, we continuously monitored the songs of the individually housed animals from 7-20 days pre-injection to 60-100 days post-injection (dpi) using sound-isolated chambers. In control animals, the song did not change at any time after the viral injection. For the first 24-48 hours after injection, the song of TeNT-treated animals was virtually identical to their original song. However, starting at 2-5 dpi, the song of TeNT-treated animals began to degrade, both in its acoustic and temporal features (Figure 1A). By 10 dpi, the song of TeNT-treated animals was highly degraded and bore no resemblance to the original song before viral injection (Figure 1 A).

During the first few days of song degradation, TeNT-treated animals produced instances of syllables with abnormally long durations far outside the range of any adult syllable duration observed in control animals (Figure 1A shows one such vocalization at 5 dpi; examples of syllable length distribution are shown in

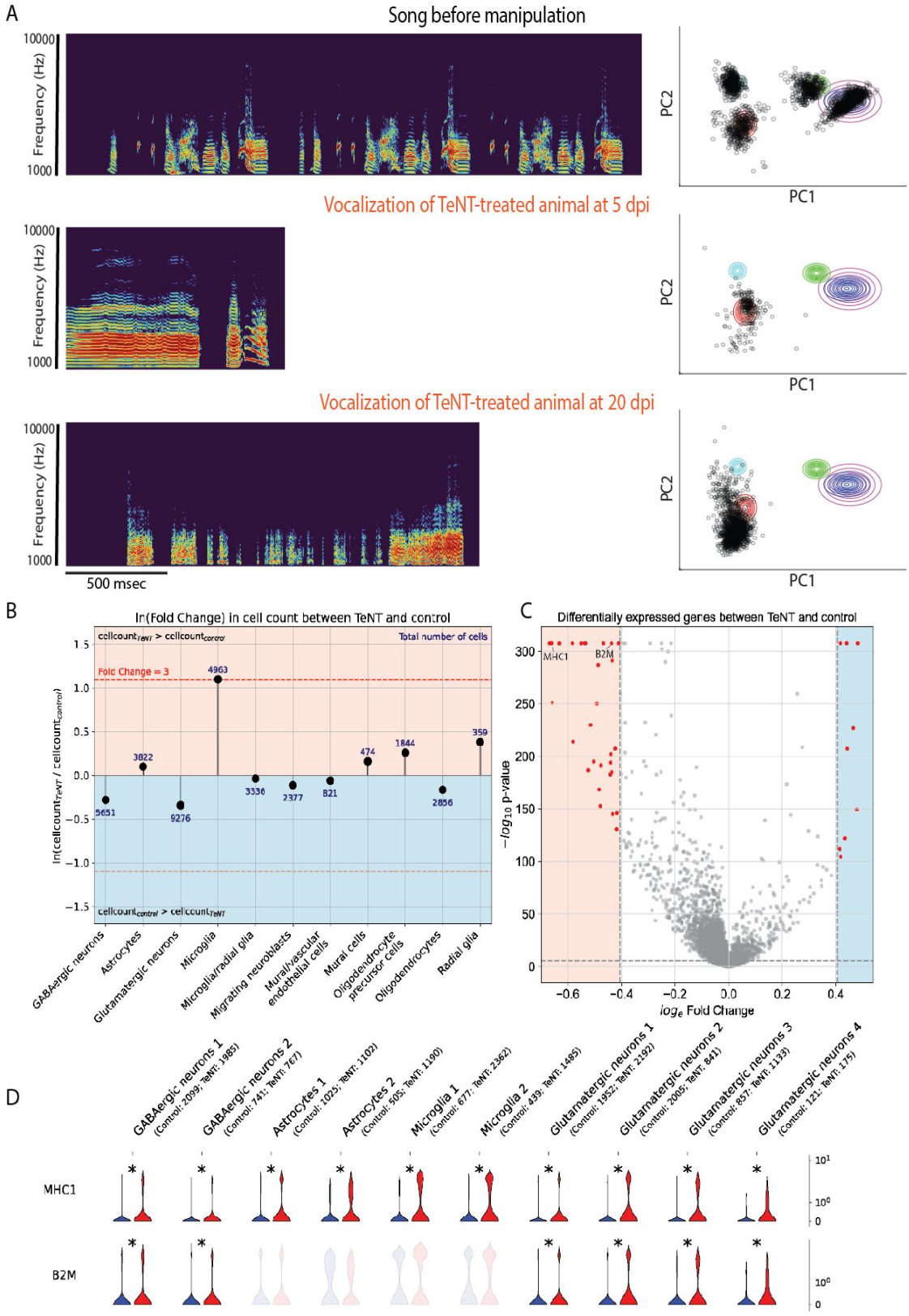

Figure legend on next page.

Figure 1: *Song degradation and transcriptomic changes after chronic inactivation of inhibitory neurons in HVC by viral expression of tetanus toxin (TeNT).* ***A (left)*** *Examples of spectrograms of songs produced by an animal treated with TeNT before, and 5, 20 days post- injection (dpi). Data from this animal (V648) are also shown in B-E.* ***A (right)*** *2D principal component analysis (PCA) visualization of syllables aka song segments produced by the animal on the same day as the spectrogram example on the left. Note: even when the songs are degraded, we continue to refer to an uninterrupted length of vocalization as a 'syllable or song segment'. Individual dots indicate single syllable renditions. In the unperturbed song (before virus injection), syllables cluster into distinct groups. See Methods for description of acoustic features used in the PCA space.* ***B*** *Log-fold change in total number of cells per cell type between TeNT-treated and control animals.* ***C*** *Volcano plot showing statistical significance over magnitude of change of differentially expressed genes between TeNT-treated and control animals across all cell types. Dotted lines indicate fold change = 1.5 and p value = Bonferroni corrected alpha of 0.05. A list of all differentially expressed genes can be found here: https://github.com/lauraluebbert/TL_2023.* ***D*** *Violin plots of normalized counts of major histocompatibility complex 1 α chain-like (MHC1) (ENSTGUG00000017273.2) and beta 2 microglobulin-like (B2M) (ENSTGUG00000004607.2) genes in control (n=2, blue) and TeNT-treated (n=2, red) animals per cell cluster. A star indicates a significant increase in gene expression in TeNT-treated animals compared to control ($p < 0.05$ and fold change > 1.5).*

Supplementary Figure 1). Later (8 to 30 dpi), all vocalizations became very short (< 100 msec) with inter-syllable intervals of varying lengths (100 msec to 1 sec) between them (spectrogram examples in Supplementary Figure 2). At 20-30 dpi, the song of TeNT-treated animals was highly variable between renditions and lacked the normal organization of motif and bout (Figure 1 A).

Our previous publication with genetic silencing of projection neurons showed a temporary degradation of the song that recovered within about 2 weeks[12–14]. However, we observed that after genetic muting of HVC interneurons, the song was completely degraded at 2-3 weeks, and bore no resemblance to the original song. Based on these observations, we concluded that although inactivation of projection neurons leads to song degradation and recovery, the permanent loss of inhibitory tone in HVC caused an irreversible inability of these animals to resume proper song production.

To investigate cellular mechanisms that might underlie the observed changes in behavior at the transcriptomic level, we performed single-cell RNA sequencing (scRNA-Seq) of HVC from control (n=2) and TeNT-treated (n=2) adult male zebra finches at 25 dpi, around the time of peak song distortion. HVC from both hemispheres of all four birds were dissected based on retrograde tracer fluorescence and dissociated to prepare single-cell suspensions, which were indexed and pooled. This allowed the construction of a combined dataset containing results from all animals and conditions without the need for batch correction (Supplementary Figure 10, Supplementary Table 2). Following quality control, we retained a total of 35,804 single-cell profiles spanning four individuals, consisting of two control and two TeNT-treated animals.

While cell type abundance was highly concordant between replicates of the same condition (Supplementary Figures 10, 16A), we found that animals treated with TeNT displayed a three-fold increase in the number of microglia (Figure 1B). In addition, we found a significant increase in the expression of the α chain of major histocompatibility complex class I (MHC I) and β_2-microglobulin (B2M) genes across several neuronal cell types in TeNT-treated animals (Figures 1 C and D). It is unlikely that this increase in microglia and MHC I was due to an inflammatory reaction caused by the surgical procedure or the AAV injection because control animals also received a viral injection with

an identical viral backbone that only expressed a fluorescent protein (NeonGreen), which did not affect neuronal activity. Thus, we hypothesize that the increase in microglia and MHC I in TeNT-treated animals is a consequence of the chronic muting of inhibitory neurons.

We confirmed the increases in MHC I by in situ hybridization (ISH) (Supplementary Figures 12 C, 13 E, and F). MHC class I molecules are heterodimers that consist of two polypeptide chains, α and B2M, and are involved in antigen presentation for T cells [15]. MHC I and B2M have been observed in previous studies to be highly expressed in neurons during brain development [16,17], consistent with a hypothetical role in synaptic plasticity[18,19]. Moreover, a human study of epilepsy observed an increase in MHC I in neurons and glial cells[20]. Here, we observe that MHC I and B2M are upregulated in response to perturbation of neuronal activity in a fully formed circuit, suggesting their possible role in synaptic changes after chronic loss of inhibitory tone.

Previous works have shown that microglia are involved in the synaptic reorganization of brain circuits, especially during postnatal development in mammals[21–23]. It has been suggested that the increase in microglia during development may be required to prune synapses, which in turn may be necessary to fine-tune the circuits so that they can attain an appropriate architecture. Our finding of an increase in the number of microglia caused by chronic silencing made us wonder whether this phenomenon may be involved, as during brain development, in a synaptic reorganization of HVC to adjust its properties.

143 **Near-perfect behavioral recovery after prolonged zebra finch song degradation and return to**
144 **control-like microglia numbers**
145 HVC interneuron silencing caused a drastic degradation of the song such that by 2-3 weeks, none of
146 the structure of the song was recognizable. Interestingly, even 3 weeks after the manipulation, the song
147 was still highly variable, even between renditions produced during the same day. This is unlike the
148 vocalizations observed after other irreversible forms of song circuit manipulations, such as
149 tracheosyringeal nerve resection or deafening, which produce songs that eventually become degraded
150 but stable between renditions [14,24–26].
151 We wondered whether the songs from animals in which we permanently inactivated inhibitory neurons
152 would eventually stabilize into a fixed degraded song or, alternatively, whether the song would keep
153 changing without ever stabilizing. Surprisingly, after 40-70 days of degraded song production, the
154 structure of the song started to re-emerge. By around 70 dpi, the song of all TeNT-treated animals was
155 highly similar to the song produced before viral injection (Figure 2A).
156 Next, we asked whether the observed transcriptomic changes at 25 dpi persisted after song restoration.
157 To this end, we performed ISH using a probe against RGS10, a gene expressed in microglia, at 25 dpi
158 (when the song is fully degraded) and at 90 dpi (after the song has recovered). At 25 dpi, the number
159 of microglia was greatly increased in TeNT-treated animals compared to control (Supplementary
160 Figures 12 A, 13 A, and B), and returned to control levels by 90 dpi. These findings suggest that
161 microglia might participate in some form of synaptic reorganization triggered by the perturbation of
162 neuronal activity caused by the permanent muting of interneurons. Consistent with this hypothesis,
163 previous epilepsy studies found upregulation of microglia associated with neuronal reorganization
164 following seizure-like activity in mammals[27,28].
165 To further investigate the hypothesis that microglia may be associated with circuit reorganization
166 involved in neuronal plasticity, we counted the number of microglial cells in HVC at different times
167 during song learning in naive (untreated), juvenile birds using ISH. The number of microglia in the
168 HVC of juveniles was higher during the early stages of the song learning period (20-50 days post-
169 hatching (dph)), compared to 70 dph, after the song became more stereotypic (Supplementary Figures
170 12 B, 13 C and D). These observations indicate that microglia may play a role in the fine-tuning of
171 brain circuits so that they achieve their appropriate architecture and function, both in young animals
172 when animals are learning a song, and in adults when perturbed circuits reorganize such that the
173 behavior can be restored.
174 **The degree of song distortion is correlated with the presence of large-amplitude voltage**
175 **deflections in HVC during nighttime**
176 Our experiments revealed that permanent inactivation of a large fraction of inhibitory neurons in
177 HVC caused a drastic degradation of the song, and its eventual recovery after more than 60 days. To
178 further understand how this perturbation caused song degradation and recovery, we decided to study
179 how the neuronal dynamics within HVC respond to prolonged behavioral perturbation due to the
180 loss of inhibitory tone.

To investigate the electrophysiological changes in HVC that accompany song degradation due to permanent loss of inhibition and subsequent behavioral recovery, we continuously recorded electrical activity in HVC across the entire duration of song degradation and recovery (0-90 dpi).

We implanted a 4-shank electrode array containing 16 recording sites in control and TeNT-injected animals. We simultaneously collected electrophysiological, head movement (recorded with the accelerometer built into the head stage), and audio recordings over a period of 90 dpi. We analyzed the spectral decomposition of the local field potentials (LFPs) during song production from an average of five vocalization epochs [29,30] (Supplementary Figures A and B). LFP recordings provide a readout of local electrical activity originating from synaptic events and action potentials[31]. In control animals, as expected, both the song behavior and LFP characteristics remained stable: the electrical activity during singing showed voltage deflections of small amplitude, which were present throughout the song.

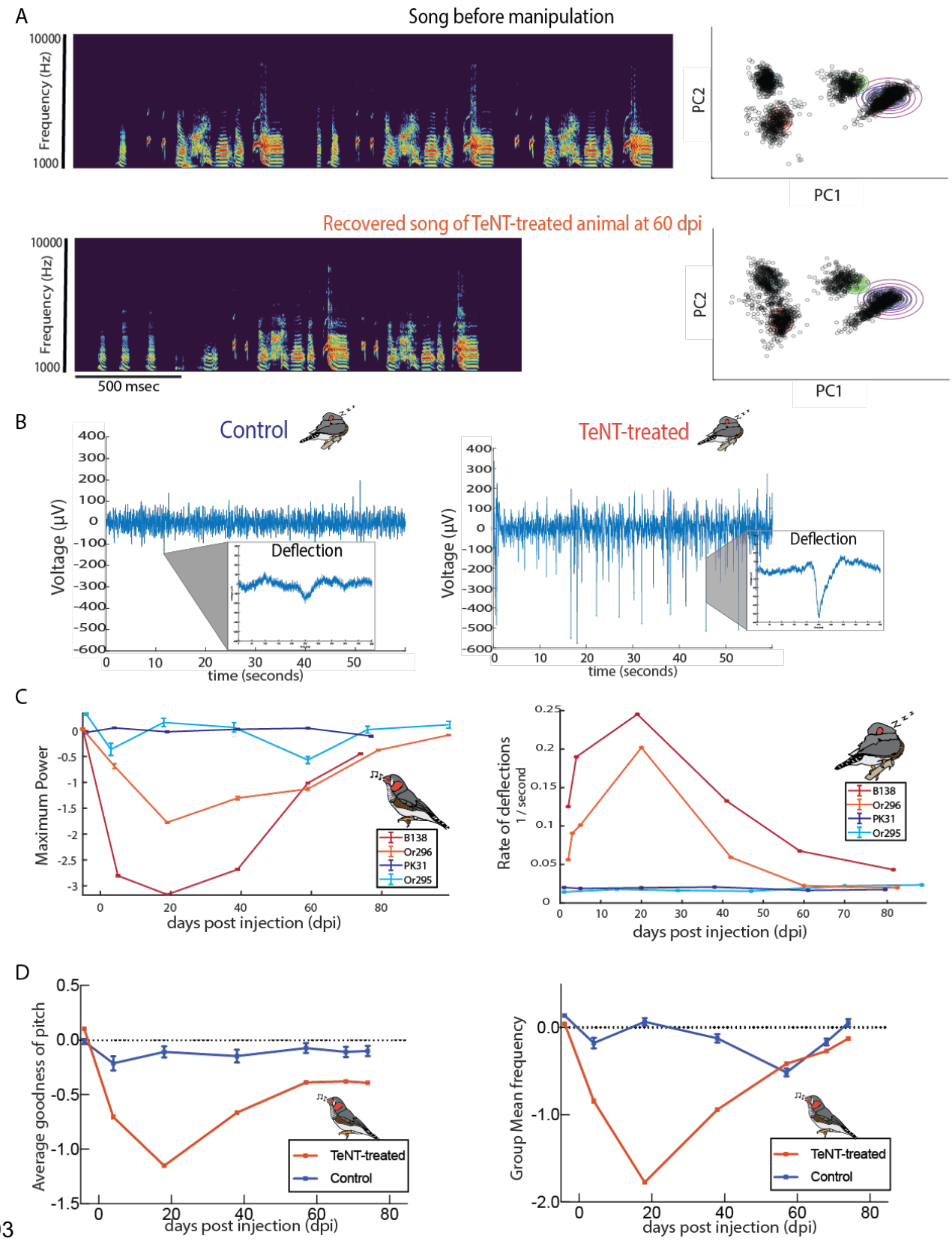

Figure legend on next page.

Figure 2: *Chronic electrophysiology recordings within HVC after chronic inactivation of inhibitory neurons by viral expression of TeNT.* ***A (left)*** *Examples of spectrograms of songs produced by an animal treated with TeNT before, and 60 days post- injection (dpi). Data from this animal (V648) are also shown in B-E.* ***A (right)*** *2D principal component analysis (PCA) visualization of syllables aka song segments produced by the animal on the same day as the spectrogram example on the left. Note: even when the songs are degraded, we continue to refer to an uninterrupted length of vocalization as a 'syllable or song segment'. Individual dots indicate single syllable renditions. In the unperturbed song (before virus injection), syllables cluster into distinct groups. See Methods for description of acoustic features used in the PCA space.* ***B*** *Raw electrophysiology traces during night time (lights off period) from TeNT-treated and control animals 5 days post-injection (dpi). Note: electrodes were implanted on the same day of viral injection. Insets show examples of stereotypical deflections that at 5 dpi were approx. 50 ms in duration, and -530 µV in amplitude, in TeNT-treated animals, compared to 96 ms and -140 µV in control animals.* ***C (left)*** *Quantification of song quality of chronically implanted animals over time. Control animals (PK31 and Or195) are depicted in shades of blue. TeNT-treated animals (B138 and Or296) are depicted in shades of orange and red.* ***C (right)*** *Rate of deflection events during night time. Control animals (PK31 and Or195) are depicted in shades of blue. TeNT-treated animals (B138 and Or296) are depicted in shades of orange and red. The highest rate of sleep voltage deflections in TeNT-treated animals occurred during the periods when the songs were most degraded, as shown on the left.* ***D*** *Different features of the vocalizations averaged/grouped before and after stereotaxic injection of control (GFP-expressing) or TeNT virus. The grouped mean frequency and goodness of pitch measures represent averages over song segments. Control animals (Or295 and PK31) are labeled in shades of blue (n=2); TeNT-treated animals (V648, B183, B138 and Or144) are labeled in shades of red and orange (n=4). Traces indicate averages over syllables sung within the 3 closest days of recorded vocalizations. Error bars indicate standard error. Values are normalized relative to distributions 5 days before perturbation (see Methods).*

(Supplementary Figure 6 B). In contrast, at 5 dpi, TeNT-treated animals produced abnormally long vocalizations that were preceded by large voltage deflections, neither of which were observed in control animals (Supplementary Figure 6 A). Between 10 to 70 dpi, the songs of TeNT-treated animals were highly variable between renditions and between days. As a result of this instability in behavior, the vocalizations of perturbed animals could not be reliably aligned across trials. Hence, we focused on electrophysiological events occurring during nighttime (lights-off periods when the animals are not moving or singing), because they showed higher consistency (Figure 2 B). The neuronal activity recorded during the nighttime period will be referred to as "offline" or "lights-off" throughout this manuscript.

Previous studies have hypothesized that HVC offline activity may reinforce the maintenance of adult song and could drive song learning in juveniles [32–36]. Therefore, analyzing electrophysiological activity in HVC during offline periods throughout the perturbation could reveal disruptions related to degraded behavior. The recordings in TeNT-treated animals during lights-off offline periods contained voltage deflections that were more frequent and of larger amplitude than those of controls (Figure 2 B, Supplementary Table 1B), similar to the electrophysiological differences observed between virus-treated and control animals during singing. In addition, in TeNT-treated animals, these large amplitude deflections at night occurred more frequently when the song was most degraded (Figure 2 C). At 5 dpi, these voltage deflections had an average amplitude of around -530 µV and -140 µV in TeNT-treated and control animals, respectively, a 280% increase in TeNT-treated animals (Supplementary

Table 1). In TeNT-treated animals, the lights-off offline voltage deflection rate returned to those seen in control as the song regained stereotypy around 50 dpi (Figure 2 C).

To further characterize these voltage deflections, we analyzed the LFPs (1-200 Hz) during the voltage deflection events occurring during lights-off periods, and we performed spectral decomposition of the LFPs. At 5 dpi, we observed increased power in the low gamma band (30-70 Hz) in TeNT-treated animals, which returned to control levels as the songs regained stereotypy (Supplementary Figure 6 C and D).

These findings suggest a relationship between the return to control-like offline electrophysiological activity and behavioral recovery. Previous studies mentioned some form of replay[33,34] in HVC during sleep; here, we show that the activity during offline periods may correlate with the quality of song execution.

Spontaneous local neuronal activity in HVC and RA during nighttime show opposite trends upon chronic interneuronal perturbation in HVC

To examine local neuronal activity at single-neuron resolution throughout song degradation and recovery, we used high-density silicon probes (Neuropixels)[37,38] to simultaneously record neurons in HVC, RA, and intervening brain areas (Figure 3 A). As described above, we obtained the most reliable measurements of abnormal brain activity in TeNT-treated animals during lights-off periods. Therefore, we performed Neuropixel recordings in head-fixed animals when the lights were off during their natural sleep cycle. To achieve the best possible signal-to-noise ratio, which would allow for single-neuron resolution, we focused on acute recordings that were obtained within a few hours after probe insertion. We performed acute recordings at 3-6, 20-22, and 70-77 dpi in TeNT-treated animals, and at 10 and 30 dpi in control animals to get a snapshot at that time window into both the behavior and the neuronal activity. We also included recordings from one naïve animal (not injected with any virus) to control for potential artifacts caused by the surgery or viral injection.

As a result of the loss of inhibitory tone, we observed seven events resembling seizure-like activity in HVC (n=3 TeNT-treated animals at 3-20 dpi), which propagated downstream into RA (Supplementary Figure 9 B). These periods of elevated neuronal firing in TeNT-treated animals in the early days after perturbation suggest that the removal of inhibitory tone acutely leads to bursts of hyperactivity that resemble discharges previously reported during seizures[1,2,39].

Next, we investigated overall activity levels to measure the overall HVC and RA dynamics after perturbation. In TeNT-treated animals, for the first 3-4 dpi, HVC started out with a heightened level of spontaneous nighttime activity (likely due to the loss of inhibition), but after 20 dpi, activity decreased to a level below that of control animals (Figure 3 B). Surprisingly, even after the song was fully recovered, by 70 dpi, the activity in HVC remained substantially reduced relative to the control ($p = 0.57*10^{-11}$) (Figure 3 B). While activity in HVC was initially elevated and eventually decreased, RA showed the opposite trend (Figure 3 B). This observation is consistent with a prior study[40] that showed acute changes in RA firing patterns in single neurons upon stimulation of HVC in brain slices, suggesting that HVC may directly increase the activity of RA interneurons. According to this model, an increase in overall activity in HVC (caused by blocking of HVC interneuron activity) would activate interneurons in RA, thereby reducing overall activity in RA. However, it is important to note

that our recordings in RA do not allow us to identify whether the recorded activity originated from excitatory or inhibitory neurons.

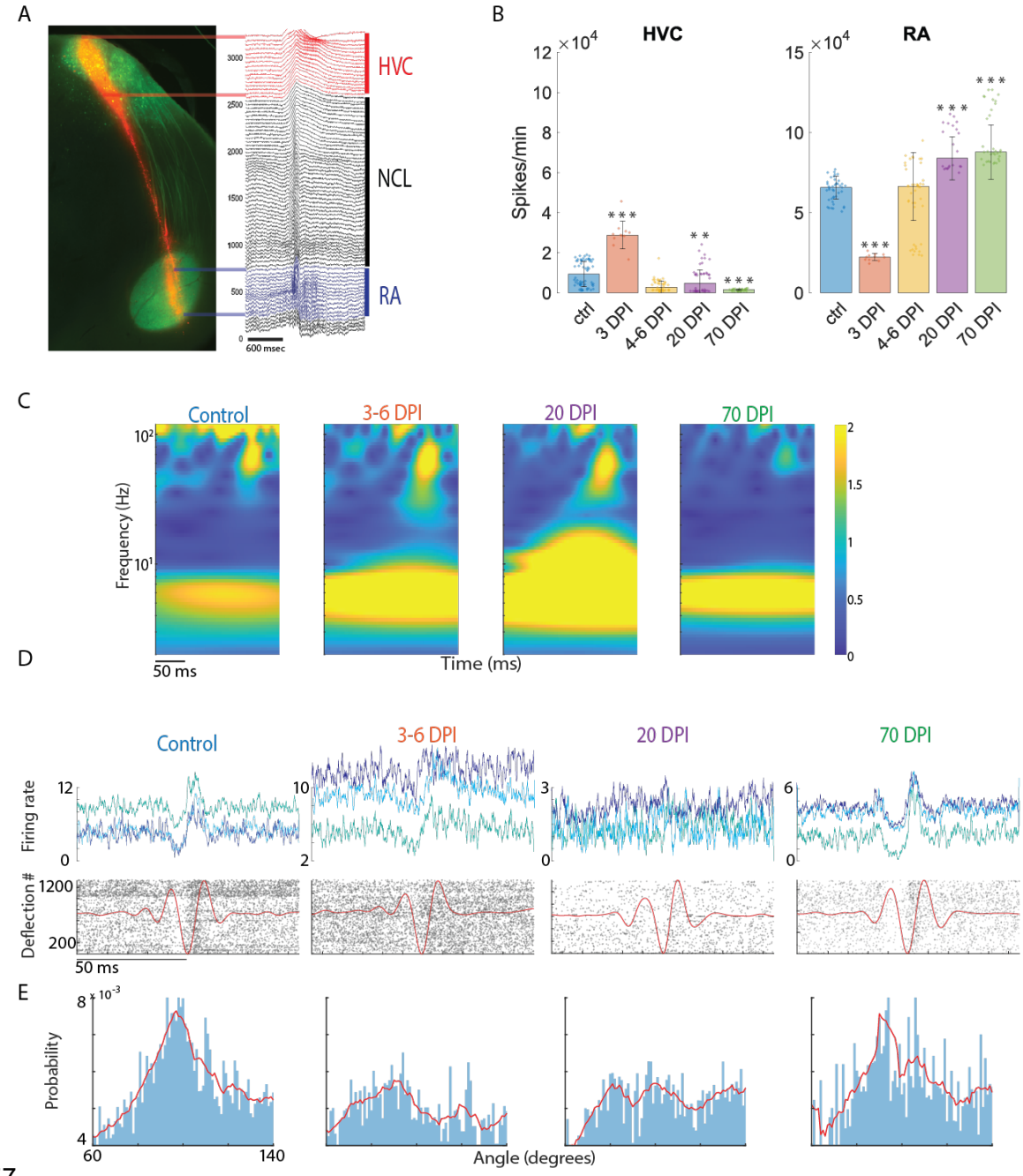

Figure legend on next page.

Figure 3: *Acute electrophysiology recordings and behavioral feedback manipulation after chronic inactivation of inhibitory neurons in HVC by viral expression of TeNT.* ***A*** *A histological section example of a brain slice from a control animal shows the track of the probe (NPIX coated with DiI) insertion (red) and GFP from the viral injection (green). Note: There is green signal in RA because the control animal received injection of a virus in which GFP is driven by the ubiquitous promoter CAG in HVC. This virus infects all cell types in HVC, and axons from HVCRA neurons innervate RA. The raw electrophysiology traces are color-coded by brain area (HVC in red, NCM in black, RA in blue).* ***B*** *Average firing rates of neurons within HVC and RA in control animals (n=3) and TeNT-treated animals at 3 (n=1), 4-6 (n=4), 20 (n=4) and 70 (n=4) dpi. In HVC, the increase in average firing rate at 3 dpi after TeNT injection significantly differs from control (p-value from rank sum test: $0.4*10^{-6}$), as well as the decrease in average firing rate after TeNT injection at 20 dpi ($p = 0.002$) and 70 dpi ($p = 0.57*10^{-11}$). In RA, the decrease in average firing rate at 3 dpi significantly differs from control ($p = 0.43*10^{-6}$), as well as the increase in average firing rate at 20 dpi ($p = 0.09*10^{-9}$) and 70 dpi ($p = 1.45*10^{-13}$). The stars above the bar plots indicate statistical significance (* = $p < 0.005$, ** = $p< 0.01$, *** = $p < 0.001$).* ***C*** *Examples of neuronal activity in a control animal, TeNT-treated animals at 3 and 20 dpi. The red arrows highlight the "superbursts" or extreme firing levels within HVC and RA which we observed in 3 animals (two animals at 3-4 dpi and one at 20 dpi) in a total of seven instances.* ***D*** *Spectral decomposition of LFPs of the average normalized deflections during lights-off acute recordings in control animals and TeNT-treated animals at 3-6, 20, and 70 dpi.* ***E (top)*** *Example traces of the firing rate of three individual neurons during deflection events that lock or do not lock to a specific phase of the alpha oscillation (shown in red in bottom plots) in HVC of control animals and TeNT-treated animals at 3-6, 20, and 70 dpi.* ***E (bottom)*** *Examples of neuronal firing (indicated by black dots) for one neuron per condition in HVC.* ***F*** *Probability distribution of the phase of firing events relative to the alpha oscillation of the LFP in control animals and TeNT-treated animals at 3-6 dpi (n=4), 20 dpi (n=4), and 70 dpi (n=2 animals). Neuronal firing precision at specific angles (60-140) of the alpha oscillations are lost or broadened in TeNT-treated animals between 3-20 dpi and re-emerges at 70 dpi, upon song recovery.*

Song stereotypy recovers despite the persistence of increased power in the alpha range oscillations and decreased offline HVC activity.

We used acute Neuropixel recordings to analyze the neuronal firing, specifically during the offline voltage deflection events, similar to those we initially observed using chronic recordings (Figure 2B). Examples of averaged voltage traces of offline deflections recorded in the acute dataset are shown in Supplementary Figure 7. Compared to the spectral composition of the LFP signature of voltage deflections observed in the chronic recordings (Supplementary Figure 6 C and D), in acute Neuropixel recordings, we detected similar changes in amplitude, power, and phase measured by the wavelet coefficient (Figure 3 C). In the LFP decomposition (continuous wavelet transform[41]) of deflection events detected in these acute recordings, we observed large differences between TeNT-treated and control animals in the alpha (1-10 Hz) and the low gamma (30-40 Hz) frequency ranges (Figure 3 C). We calculated the difference in power from the estimated spectral density (periodogram) between the averaged (per animal) deflection and non-deflection events in the alpha (1-10 Hz) and low gamma (30-40 Hz) range. In the low gamma range (30-40 Hz), after an initial increase, the power returned to control levels at 70 dpi (Supplementary Figure 9 A). The relative phase between the alpha and low gamma oscillations during voltage deflections initially varied in angle, then returned to resemble controls by 70 dpi (Supplementary Figure 9 C-E). In contrast, the power in the alpha range stayed significantly higher in TeNT-treated animals, even after the song recovered at 70 dpi (Supplementary Figure 9 A).

Next, we compared the timing of single neuron firing with the phase of the alpha and low gamma oscillations during offline voltage deflection events. To this end, we turned to methods previously

described to characterize sharp-wave ripple events during offline activity in the hippocampus [42]. We found that in control animals, the neuronal firing within HVC locked tightly to specific phases of the alpha and low gamma oscillatory events during offline voltage deflections (Figure 3D and E). In TeNT-treated animals, during the song degradation period, the precision of firing with respect to low gamma oscillations in HVC or to alpha and low gamma oscillations in RA during deflection events did not change compared to control (Supplementary Figure 8). However, during the song degradation period, the precision of local neuronal firing to alpha oscillations between 60 to 140 degrees was lost or broadened compared to control and song-recovered animals (Figure 3 D and E). As song stereotypy was regained, the locking of firing to specific phases of the alpha oscillations during deflections re-emerged (Figure 3 D and E).

The finding that the neuronal firing precision locked to alpha frequency oscillations returned to control-like is unexpected, given that the power in this frequency range remained elevated even after the song recovered. Sixty days after the perturbation, the animals were able to produce a normal song despite a persistent increase in alpha power an overall decrease in HVC, and an increase in RA spontaneous single-neuron activity, respectively.

In sum, we found that restoration in behavioral stereotypy was paralleled by an increase in neuronal firing precision to low-frequency oscillations. However, even after the song recovered, we see long-term changes in the LFP power and offline HVC dynamics that point to large-scale restructuring in total population activity within HVC. These observations indicate that the adult brain can overcome a permanent inactivation of a significant fraction of inhibitory neurons, which causes extended periods of abnormal activity, and precisely restore a complex behavior without recovering the original neuronal dynamics. This suggests that this circuit can transition into a new state capable of producing the original behavior despite the persistence of abnormal neuronal dynamics.

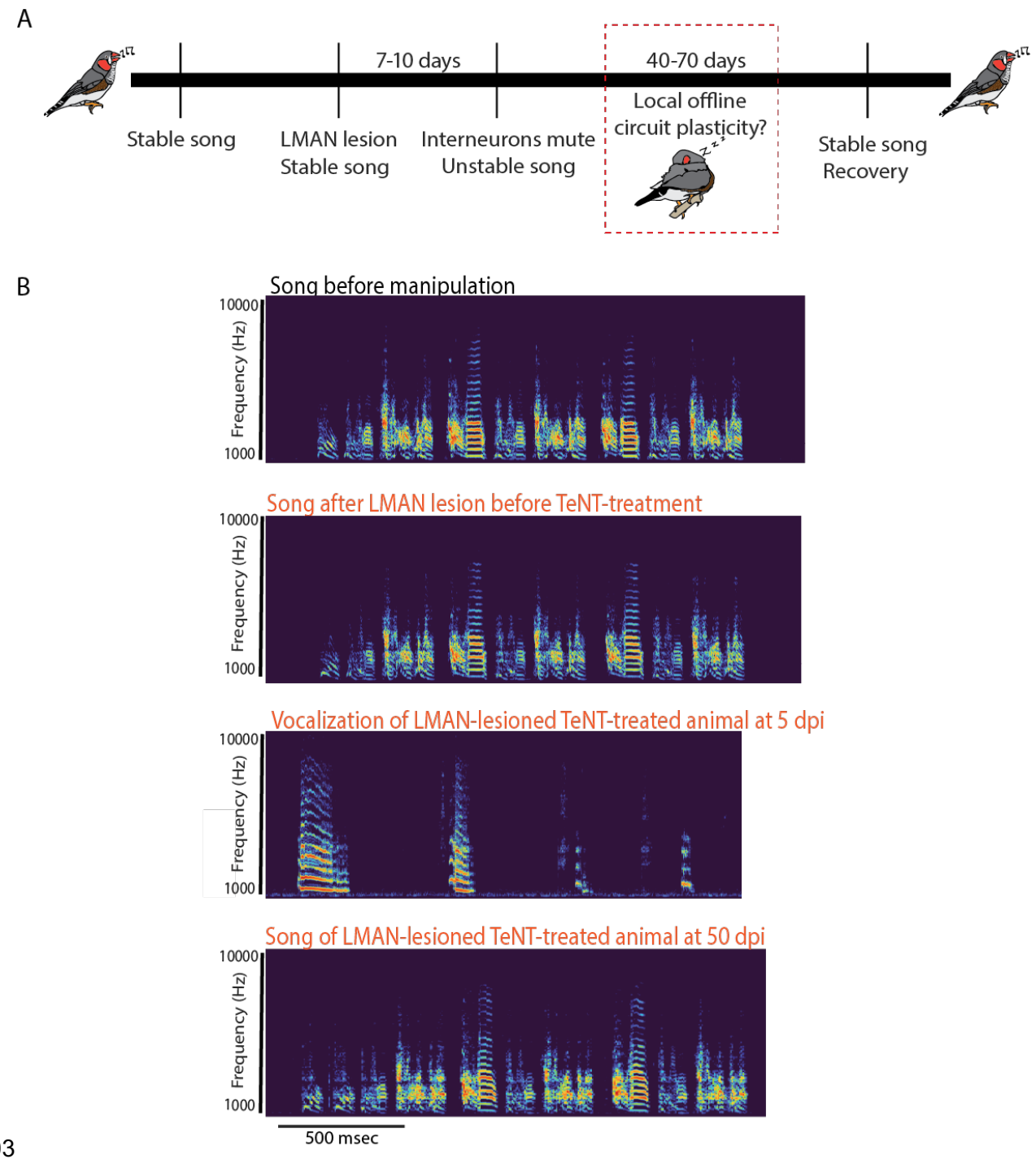

Figure 4: *Song degradation and recovery after chronic removal of inhibition in an animal without LMAN. PK72 animal. Spectrograms are showing the song of the animal before and after LMAN lesion at 5 and 50 days after viral injection (dpi). Supplementary Figure 5 shows histology and additional spectrograms of the same animal.*

306 **Permanent genetic muting of inhibitory neurons in HVC leads to zebra finch song degradation**
307 **and recovery that does not require a brain nucleus essential for song learning**
308 The observed increase in microglia both in juvenile animals while they are learning the song, and in
309 adult animals after HVC perturbation suggests the possibility that some of the mechanisms mediating
310 song recovery in adults and song learning in young animals may be shared. To test this hypothesis, we
311 asked whether adult song recovery after manipulation of interneurons required a key brain nucleus
312 that is essential for song learning.
313 Juvenile animals start singing a highly variable and unstructured song, and by continuous trial and
314 error over 2-3 months and thousands of practice renditions, their song "crystallizes" into a stable motif
315 with minimal variability[43,44]. Song learning in juveniles requires the lateral portion of the
316 magnocellular nucleus of the anterior neostriatum (LMAN), another nucleus in the song system that
317 provides input to RA, the downstream target of HVC[45–47]. During learning, LMAN injects noise into
318 RA to enable the exploration of different states[48] and gates the plasticity of synapses from HVC to
319 RA[49]. In addition to its role in learning, LMAN is also necessary for song modification in adult
320 animals[50]. Deafening adult animals causes a progressive degradation of their songs over several weeks,
321 which can be blocked by prior LMAN lesioning. Similarly, a previous study demonstrated that small,
322 focal electrical lesions in HVC in adult animals caused their songs to degrade which can be prevented
323 by lesioning LMAN[13]. Therefore, it is possible that when HVC is perturbed in adult animals, the
324 'noisy' input from LMAN to RA becomes more dominant than the input from HVC, and this causes
325 degraded song production. To test this hypothesis, first, we chemically lesioned LMAN by bilateral
326 ibotenic acid injection, and 10 days later, we injected AAV-dlx-TeNT into HVC (n=3). We observed
327 that in animals with AAV-dlx-TeNT injection into HVC of animals with a prior LMAN lesion, the
328 song degraded and recovered in a similar way and same time-scale, as animals with intact LMAN,
329 indicating that song degradation after HVC perturbation is not caused by an exacerbated LMAN
330 influence on the song system (Figure 4 & Supplementary Figure 3-5). Our finding that animals
331 degraded and recovered their song without LMAN indicates that it does not cause the degraded song
332 production or is necessary for the song recovery after HVC interneuron perturbation. This result is
333 surprising given our observations indicating that the spontaneous RA offline activity exhibits
334 significant changes during the degradation and recovery process, which, based on previous work[51,52],
335 would require some re-tuning of RA properties involving LMAN. These findings indicate that the
336 recovery following perturbation of interneurons in HVC in adults likely occurs by mechanisms
337 different from song learning in juveniles, which requires the LMAN nucleus[46,53].

338 ## Discussion

339 The brain must balance excitation and inhibition to maintain physiological activity patterns and enable
340 reliable behaviors. We found that permanently muting a significant fraction of inhibitory neurons in a
341 pre-motor circuit in adult songbirds severely disrupts their song, a complex, learned behavior for an
342 extended period (40-70 days). However, despite this long-term disruption, animals eventually
343 recovered and produced a song that was highly similar to the original.
344 We investigated the transcriptomic and electrophysiological changes induced by this perturbation to
345 understand the cellular mechanisms responsible for this behavioral recovery. First, we explored the

transcriptomic changes during song degradation and recovery. We found a 3-fold increase in microglial marker genes in our sc-RNAsequencing data compared with control animals. This increase was confirmed via ISH and shown to return to control levels as the song recovered. Microglia are known to play a role in synaptic changes during learning and circuit establishment [21–23], and consistent with these previous works, we found an increase in microglia during song learning in juvenile birds. Moreover, several works have shown an increase in microglia after seizures in rodents and humans[27,28,54]. Our study suggests that microglia may also be involved in restoring function in the adult brain.

We performed long-term electrophysiological recordings in HVC during song degradation and recovery. We detected changes in voltage deflection events as a readout of offline dynamics (during the lights-off period) within HVC. We observed an increase in the rate and amplitude of these deflection events during song degradation, which returned to control-like once the song regained stereotypy. To investigate the offline dynamics with higher resolution, we investigated single and multi-neuronal activity within HVC and its downstream nucleus RA. After muting interneurons in HVC, we observed two changes in HVC dynamics that remained abnormal even after the song had fully recovered: a decrease in offline single neuron firing and an increase in alpha frequency power. Synaptic inputs could cause alpha-frequency LFP signals in a brain region[31]. In our experiments, the decrease in neuronal firing in HVC that we observed may have triggered a compensatory increase in the synaptic inputs originating from upstream nuclei projecting into HVC (such as Uva and Nif), which could account for the observed increase in alpha power. Alternatively, this increase in alpha power could originate from synaptic inputs from neurons within HVC. Future experiments will be necessary to understand how the perturbations of HVC affect the dynamics of other nuclei in the song system.

To investigate the relationship between HVC oscillations and local neuronal dynamics, we measured the precision of single neuronal firing to specific phases of alpha and gamma oscillations, where we observed significant changes upon muting of inhibitory neurons. In control animals, single neuronal activity within HVC showed precise firing to certain phases of alpha and gamma oscillations during offline voltage deflections. In contrast, after interneuron muting, during the peak song distortion, single neuronal firing did not align to specific phases of alpha frequency oscillations. Then, as the song recovered, the precision of firing to the phase of alpha oscillations returned to normal.

The relationship between single neuronal firing and alpha oscillations in the song system is not understood, but it could represent how the local HVC circuit responds to inputs from other brain areas. One hypothesis consistent with our observations is that during song degradation when stereotypy of the behavior is lost, the local HVC circuit is unable to properly respond to synaptic inputs, which could result in the observed desynchronization of spikes to alpha oscillations. As the song comes back to normal, the precision of local neuronal firing recovers even though the power stays permanently elevated in the alpha range. These findings suggest that the motor circuit is able to execute behavior properly even in the face of permanent changes to its properties, such as increased alpha frequency power and low spontaneous offline neuronal activity in HVC.

Our experiments suggest that the song recovery in adults following HVC interneuronal perturbation has some superficial similarities, such as variable song production and an increase in microglia

numbers, to the process by which juveniles learn their songs. However, we found that there is a fundamental difference between these two processes. In juveniles, song learning requires that LMAN provides input to RA, and it has been hypothesized that LMAN injects noise into RA such that inputs from HVC into RA can explore different states[45,55]. Moreover, previous works indicate that LMAN is also required to enable song changes even in adults [52,56]. In contrast, here we found that recovery after chronic genetic muting of inhibition in HVC can occur without LMAN. These observations reveal that the adult brain's mechanisms to recover behavior after disruptions in neuronal activity are fundamentally different from those used to acquire the behavior as juveniles.

We wondered if the mechanisms of behavioral recovery in an adult are similar depending on whether the activity of excitatory or inhibitory neurons is selectively perturbed. In a previous publication, we observed that permanent genetic muting with TeTN of a large fraction of projection neurons in HVC led to a degraded song, which recovered in around 2 weeks[12]. In this work, we observe that permanent genetic muting of a large fraction of interneurons also leads to degradation and recovery of the song, albeit the recovery takes around 2 months in this case. Taken together, our previous work and this study show that HVC is able to restore functional dynamics after two "orthogonal" perturbations to the circuit, highlighting the resilience of this nucleus. Our results indicate that HVC can still precisely execute song production, a complex learned behavior, despite a significant reduction in the fraction of active inhibitory neurons and an overall abnormal activity in HVC.

These findings suggest that the successful functional recovery of behavior after a severe and prolonged brain perturbation can occur without the restoration of the normal dynamics of the circuit. Instead, the circuit seems to adapt and reorganize into a new state capable of producing the original behavior. This adaptive process may be crucial for maintaining behavioral accuracy over long periods of time and could represent a key feature of brain resilience.

Methods

Animals

The Institutional Animal Care and Use Committee of the California Institute of Technology approved all procedures involving zebra finches. All birds used in the current study were bred in our own colony and housed with multiple conspecific cage mates of mixed genders and ages until used for experiments. Before any experiments, adult male birds (>120 days post-hatching (dph)) were singly housed in sound isolation cages with a 14/10 hr light/dark cycle for >5 days until they habituated to the new environment and started singing. Thereafter, birds were kept in isolation until the end of the experiment.

Behavioral recordings

Adult male zebra finches' (n=30, 130-890 dph) undirected songs were recorded 24/7 in sound-isolated chambers for 10-14 days before any manipulation to get a baseline of their song. Recordings were done with microphones (Audio-technica, AT831b) that are connected to an amplifier M-TRACK 8 and recording software Sound Analysis Pro 2011 at 44100 Hz. Animals were housed in these chambers and continuously recorded for the duration of the experiments.

Viral vectors

426 AAV-TeNT contained the promoter from the human dlx5 gene driving expression of the light chain
427 of tetanus toxin fused to EGFP with a PEST domain. AAV9-dlx-TeNT was obtained from the Duke
428 viral core facility. The control virus used was AAV9-CAG-NeonGreen, where CAG drives the
429 expression of NeonGreen, which is a GFP variant.

430 **Stereotaxic injection**

431 Birds were anesthetized with isoflurane (0.5% for initial induction, 0.2% for maintenance) and head-
432 fixed on a stereotaxic apparatus. First, to inject a retrograde tracer in area X, craniotomies were made
433 bilaterally and fluorescent tracers (fluoro-ruby 10%, 100-300 nL) were injected through a glass
434 capillary (tip size ~25 µm) into the corresponding nuclei (coordinates from dorsal sinus in mm - area
435 X: Anteroposterior (AP) 3.3-4.2, Mediolateral (ML) 1.5-1.6, Deep (D): 3.5-3.8). To deliver the virus
436 (AAV) into HVC, a second surgery was performed 7-10 days after retrograde tracer injection. By then,
437 HVC was strongly labeled by fluorescence and visible through a fluorescent stereoscope. AAVs
438 diffuse extensively (~500 µm), and a single injection (~100 nL) in the center of HVC was sufficient
439 to label enough cells. All injections in HVC were performed at ~20 nL/min to minimize physical
440 damage. At the end of every surgery, craniotomies were covered with Kwik-Sil, and the skin incision
441 was closed with Gluture.

442 <u>LMAN lesion</u>

443 We used ibotenic acid (2%) dissolved in 100mM NaOH to chemically ablate LMAN, in adult male
444 zebra finches (n=4) between 120-200 dph. Coordinates used with 50 degree head angle were
445 (3.2/3.5/3.8 mm AP; 1.7/1.8/2 mm ML ; 2.4;2.8/2.4;2.7/2.3;2.5 mm Deep). We achieved ablation of
446 ~80-98% of LMAN bilaterally confirmed by CGRP staining. We initially measured the acoustic
447 variability within each syllable before and after lesion and found that it decreased in 3/4 animals
448 (which agrees with previous findings) to confirm the success of our LMAN lesions. Next, 7-10 days
449 following the LMAN ablation we followed the previously describe stereotaxic injection protocol for
450 tracer and virus injection. The one animal that did not have decrease in syllable level acoustic
451 variability following lesion later on by histology was also confirmed to only receive a partial lesion
452 therefore we removed this animal from further behavioral analysis.

453 **Chronic electrophysiology recordings**

454 Animals (n=4, 300-700 dph) were implanted in the right hemisphere HVC with 4 by 4 electrode arrays
455 (Neuronexus A4x4-3mm-50/100-125-703-CM16LP) based on retrograde fluorescent labeling of HVC
456 (just as for viral injections). Post-perfusion histology images were obtained to locate the electrode
457 array within HVC for each animal (Supplementary Figure 15). Electrode implantation occurred within
458 the same surgery as the viral injection.

459 This procedure follows the same surgical steps as the viral delivery protocol, until the point of
460 electrode implantation. A small opening was cut on the dura (just big enough to fit the electrode array)
461 to lower the electrodes manually. The reference and ground were a gold screw pin placed into the
462 cerebellum. The skin was removed from the surface of the skull for the majority of the surface, in
463 order to secure the implant. Before implantation, the skull and the craniotomies were cleaned with
464 saline and dried and the skull was prepared according to the protocol of the C&B Metabond cement
465 system. Post implantation we covered the craniotomies with kwik-sil. Once hardened, we covered the

466 whole skull, and the part of the electrode still exposed, with metabond. The head stage (Intan RHD
467 Part # C3335) was connected to the probe before implantation and securely metabonded to the
468 connection between the probe and head stage in order to prevent detachment when the bird is moving.
469 SPI interface cables (Intan Part #C3203, #C3213) were connected to the acquisition board (Open
470 Ephys). Data was recorded at 30,000 Hz with the Open Ephys software system. Animals were freely
471 moving with a passive counterweight-based commitator system.

472 **Acute electrophysical recordings**

473 Animals (n=10, 140-250 dph) went through the same surgical procedure as described for a stereotaxic
474 viral injection. However, at the end of the surgery the skin was removed from the skull, and the whole
475 skull was pre-treated and covered in metabond except for the craniotomies over HVC that were
476 covered with kwik-cast until the day of the acute recording session. Shortly before the recording
477 session, a head-bar was glued on top of the frontal surface of the metabonded skull to allow the head-
478 fixation of the bird for the recording session. Then, the kwik-cast was removed from the craniotomy
479 over HVC (left or right hemisphere or both depending on the animal) and a small incision was made
480 in the dure over HVC, which was identified by the retrograde tracer previously injected. The ground
481 was placed into the cerebellum. Then the high-density silicone probe (Neuropixel) was lowered with
482 a motorized arm over hours for 2.6-3 mm deep into the brain. The head stage and acquisition board
483 was connected to the computer and data was recorded with the Open Ephys software. Once the probe
484 settled in the brain, we had 4 distinct recording sessions. Post-perfusion histology images were
485 obtained to locate electrode array within HVC for each animal (Supplementary Figure 16). Recording
486 sessions: lights on silence (10 min), followed by playback of the bird's own song (3-10 min); lights-
487 off silence (10 min), followed by playback of the bird's own song (3-10 min); microinjection of 100
488 nL 250 µM Gabazine (Hellobio, HB0901), followed by the same protocol of lights-off and on without
489 Gabazine.

490 **Song analysis**

491 Song analysis was performed using MATLAB (MathWorks).

492 <u>Song feature parameterization</u>

493 Continuous audio recordings (44.1 kHz) were segmented into individual bouts manually. We used the
494 open-source Matlab software package, Sound Analysis Pro 201 [57] to generate spectrograms and derive
495 non-linear, time-varying song parameterizations. The time-varying features were: pitch, goodness of
496 pitch, Wiener entropy, log-power of the spectrogram, mean frequency, and the maximum power in
497 each quadrant of the frequency range 0- 11 kHz (labeled power 1, power 2, power 3, and power 4).
498 These features were computed across the entire bout every 1 ms. These time-varying features were the
499 base from which various portions of the song were further characterized.

500 <u>Syllable parameterization</u>

501 To quantify the change in the acoustic structure of the song, we tracked song features over the course
502 of the perturbation. In Fig 1, we took the average feature values over all song segments in the three
503 closest days of recorded song for each day plotted. We extracted the average mean frequency, average
504 pitch, maximum goodness of pitch, maximum log power, minimum entropy, and entropy variance
505 over the first 50 ms of each song segment, or the entire song segment if the segment was less than 50

ms. We centered and normalized feature values by the mean and standard deviation of the distribution of feature values in syllables five days pre-perturbation to compare trends across birds.

To visualize how the population of song segments evolved relative to the original syllable structure (Fig 1B), we plotted song segments as points in the first 2 principal components of the 7-dimensional acoustic feature space composed of: average mean frequency, average pitch, maximum goodness of pitch, maximum log power, minimum entropy, and entropy variance over the first 50 ms of each song segment, and the full duration of each song segment. 500 syllables recorded pre-perturbation were labeled by hand, and contour plots were made at the mean of each labeled stereotyped syllable type for visual reference as the song degrades and recovers. Principal component dimensions were computed on the 500 labeled syllables, and subsequent song segments were projected into this principal component space.

Syllable segmentation

We identified syllables and silences within each bout by imposing thresholds on the time-varying, total log-power of the spectrogram. We selected the threshold based on manual inspection for each bird. We then performed a smoothing step wherein periods of silence less than 15 ms were converted to song segments. Song segments less than 20 ms were excluded from the analysis. Segmentation was further checked by eye by random sampling across both stereotyped motifs and degraded song. We then applied the power threshold to the entire course of song recordings for each bird.

A note on terminology: we refer to song segments to indicate continuous periods of singing. In the unperturbed song, these song segments are termed syllables. Because this is a continuous recovery process, these terms sometimes overlap in our usage.

Syllable timing distributions

Syllable durations were extracted from the syllable segmentation process. Discrete distributions of syllable durations were computed by normalizing each distribution of all song segment durations within individual days such that the sum of each daily distribution over all binned durations equaled one. Distributions for individual days were then assembled into a matrix wherein the columns represented normalized distributions for individual days. This matrix was plotted as a heat map in Supplementary Figure 1.

Continuous representation of bout trajectory

We generated continuous visualizations of bouts across the entire perturbation trajectory as shown in the graphical abstract [58,59]. We randomly sampled 100 bouts from single days of recording to build a representative sample of the song over the course of the experiment. For each bout, we slid a 150 ms window in 3 ms steps along the bout length. We then generated a high-dimensional, acoustic parameterization of each 150 ms song window by taking the moving average in 20 ms segments every 5 ms of six song features (mean frequency, pitch, goodness of pitch, power 4, power 2, and summed log power of the spectrogram). We performed principal component analysis on this high-dimensional set across all bouts to reduce the feature set to 30 dimensions.

Analysis of the chronic electrophysiology recordings

Preprocessing of Data

Bad channels were removed from the analysis by visual inspection of the first minute of each recording. Three of the four birds studied had one channel that had behavior that was an order of magnitudes larger than all others, and data from this channel was removed for further analysis. Furthermore, channels that appeared out or close to the edge of HVC based on histology were also eliminated from further analysis.

Detection of sharp waves

Accelerometer and electrophysiology data were resampled to 125 Hz from the original 30,000 Hz using the Matlab resample function. Since accelerometer data was not zero-centered, the mean was subtracted before resampling and then added back to avoid edge effects from the lowpass filtering during resampling. Sharp waves were detected from the downsampled data using a procedure adapted from a zebra finch sleep study [60] and were only detected during periods of low movement. This was determined by setting a threshold on the moving standard deviation of the velocity as movement events appeared as large fluctuations in the velocity data. Briefly, the local field potential (LFP) traces were averaged across all electrodes and bandpassed from 1 to 40 Hz using MATLAB's bandpass function. Putative events were detected by peaks in the inverted (-1x) trace and were in the lowest 5% of all values during non-movement, were at least 10 ms long, and were 80 ms apart. These putative events were used to construct a template by taking the average 80 ms trace centered on each event. Cross-correlating this template with the entire overnight LFP trace and taking the z- score (mean and SD from only non-movement times) revealed events that closely matched the template. Peaks were detected in the z-scored cross-correlation and defined as events if they were above a given threshold and were at least 80 ms apart. Notably, thresholds were not tuned across birds or recordings but a constant threshold was sufficient in all birds to detect events. Extraction of sharp waves. The detected events were used to index the original 30,000 Hz data. 500 ms of data was extracted for each event and recentered on the minimal value in the center 100 ms. An equal number of 500 ms non-sharp wave events were extracted from a random selection of times without movement or sharp waves. Sharp waves with clear electrical noise were omitted from further analysis.

Multi-unit activity (MUA):

MUA was detected using an established method [61]. Briefly, channels were common averaged referenced, bandpassed from 600 to 6,000 Hz, and upsampled to 50,000 Hz. The square root of the local energy operator (Mukhopadhyay & Ray, 1998) was taken and then Gaussian smoothed ($\sigma = 0.4$). Thresholding this trace and then downsampling back to 30,000 Hz gave the times of high MUA.

Time-frequency analysis

The continuous wavelet transform was used to compute the spectra for each sharp wave. Percent increase relative to mean power spectra were averaged within each day and bird. The spectrum of average power in the center 33 ms of each event was used to compute the percent increase in power relative to non-sharp wave events at each frequency. To determine the presence of phase-amplitude coupling between low-frequency (10-20 Hz) and gamma-frequency (30-40Hz) bursts, the phase of the low-frequency band, and power of the high-frequency band were extracted using the Hilbert transform of the band-passed signal. Determining whether the peak gamma activity occurred at a consistent phase of the low-frequency oscillation, could suggest phase-amplitude coupling. To further assess this, we asked at what time and frequency a max in the spectrum occurred for each event, relative to the minima of each sharp wave. We also wanted to ask whether the power of deflections in different

frequency bands differed significantly across control and experimental birds. We computed the relative increase in power in the frequency bands of interest (15-30 Hz, and 30-70 Hz) during a deflection relative to non-deflection times. We then used a t-test to statistically test whether power differed significantly across birds for a given day.

Analysis of the acute electrophysiology recordings

The low-frequency electrophysiology data was recorded at 2,500 Hz while the high-frequency data was recorded at 30,000 Hz. A MATLAB script was written to analyze the low- and high-frequency oscillations. All low-frequency data was high pass filtered (1-300 Hz) and median subtracted. All high-frequency data was common average referenced and low-pass filtered (300-7,000 Hz). For deflection event detection, we used two methods. One to use a template per animal for extraction of deflection and non-deflection events with template matching in a semi-automated manner. Second, manually picked out peaks that were 9 standard deviations away from the average raw signal, then further manually curated these events. Most of our further analysis was done using the deflection events that resulted from template matching (except Supplementary Figure 10A for the difference in power between deflection and non-deflection event calculation). For spike detection, we used two separate methods, one to threshold the high-frequency data to only consider spikes that are 9 standard deviations above the average signal in a 2-minute window. The second method used for spike detection was using the Kilosort software v2.5 [62] to extract spikes from the raw data. Next, we manually curated the dataset to capture the waveform and firing rate of neurons. The thresholded spiking data was used to generate Figure 3BC. We performed statistics (Wilcoxon, rank sum test) to show statistically significant firing rates related to control in HVC and RA in Figure 3B.
To calculate the power difference between deflection and non-deflection events in the acute recording in Supplementary Figure 11 A, we used a script developed for the chronic recordings with the use of the built-in MATLAB function *pwelch*. To analyze the spectral decomposition of the LFP signature (Figure 3D) in control and TeNT-treated animals during the experimental timeline we calculated the Morse continuous wavelet transform using the built-in MATLAB function. From this finding, we obtained the mean oscillation at the alpha range (1-10 Hz) and at low gamma (30-70 Hz). Then, we performed an iterative alignment process of these two oscillations and calculated the angle of the low-frequency oscillation (from obtaining the Hilbert transform) at the peak amplitude of the high-frequency oscillation (Supplementary Figure 11BC). Then we proceeded to align the single neuronal firing (obtained from Kilosort) to the alpha and the low gamma oscillations and plotted the normalized probability distribution (Figure 3F) of neurons firing at a specific phase (angle) of the alpha or low gamma oscillations. We performed the Kolgomorov-Smirnov test on the cumulative density function (CDF) (Supplementary Figure 11D) to assess if the change in probability distribution in the relationship between alpha and low gamma oscillations is statistically significant from control distributions at 3-6, 20, and 70 dpi.

Single-cell RNA sequencing

<u>Animals</u>

All of the work described in this study was approved by California Institute of Technology and Oregon Health & Science University's Institutional Animal Care and Use Committee and is in accordance

627 with NIH guidelines. Zebra finches (Taeniopygia guttata) were obtained from our own breeding
628 colony or purchased from local breeders.
629 Dissociation and cDNA generation
630 Animals were anesthetized with a mix of ketamine-xylazine (0.02 mL / 1 gram) and quickly
631 decapitated, then the brain was placed into a carbogenated (95% O2, 5% CO2) NMDG-ACSF petri
632 dish on ice. The brains were dissected on a petri dish with NMDG-ACSF surrounded by ice under an
633 epifluorescent microscope guided by the fluoro-ruby retrograde tracing from Area X to HVC.
634 We used the commercially available Worthington Papain Dissociation system with some minor
635 changes and add-on steps. We followed all the steps included in the Worthington protocol with a final
636 concentration of 50 U/mL of papain. To match the intrinsic osmolarity of neurons in zebra finches we
637 used NMDG-ACSF (~310 mOsm) instead of the EBSS for post-dissection and STOP solution.
638 Another modification was to add 20 µL of 1 mg/mL Actinomycin D (personal communication from
639 Allan-Hermann Pool; [63]) into 1 mL of the post-dissection medium and the STOP solution in which
640 trituration occurred. Papain digestion occurred for an hour on a rocking surface with constant
641 carbogenation in a secondary container above the sample vial at RT. We performed trituration with
642 increasingly smaller diameter glass pasteur pipettes. Trituation was performed inside the papain
643 solution. Then, once the tissue was fully dissociated, we centrifuged the samples at 300 g RT for 5
644 minutes and resuspended them in STOP solution. Next, we used a 40 µm Falcon cell strainer pre-wet
645 with the STOP solution and centrifuged again at 300 g RT for 5 min. Finally, we resuspended the cell
646 pellet in 60µl of STOP solution and proceeded to barcoding and cDNA synthesis. The cell barcoding,
647 cDNA synthesis, and library generation protocol were performed according to the Chromium v3.1
648 next GEM single cell 3' reagent kits by Jeff Park in the Caltech sequencing facility. Sequencing was
649 performed on an Illumina Novaseq S4 sequencer with 2x150 bp reads.
650 Generation of count matrices
651 The reference genome GCA_003957565.2 (Black17, no W) was retrieved from Ensembl on March
652 20, 2021 (http://ftp.ensembl.org/pub/release-104/gtf/taeniopygia_guttata/). We quantified the gene
653 expression in each of the four datasets using the kallisto-bustools workflow [64]. The reference index
654 was built using the kb-python (v0.26.3) *ref* command and the above-mentioned reference genome.
655 Subsequently, the WRE sequence was manually added to the cdna and t2g files generated by kallisto-
656 bustools to allow the identification of transgenic cells. The count matrix was generated for each dataset
657 using the kallisto-bustools *count* function. The resulting count matrices were compared to those
658 generated by the 10X Cell Ranger pipeline (v6.0.1) and kallisto-bustools *count* with *multimapping*
659 function. For all four datasets, kallisto-bustools mapped approximately 10% more reads than Cell
660 Ranger (Supplementary Figure 16). No increase in confidently mapped reads was observed when
661 using the multimapping function, indicating that reads align confidently to one gene in the reference
662 genome (Supplementary Figure 16).
663 Quality control and filtering
664 The datasets were filtered separately based on the expected number of cells and their corresponding
665 minimum number of UMI counts (Supplementary Figure 10). Following quality control based on
666 apoptosis markers and library saturation plots (Supplementary Figure 10), the count matrices were
667 concatenated and normalized using log(CP10k + 1) for downstream dimensionality reduction and

visualization using Scanpy's (v1.9.1; [65]) *normalize_total* with target sum 10,000 and *log1p*. Gene names and descriptions for Ensembl IDs without annotations were obtained using gget (v0.27.3; [66]).

Dimensionality reduction and normalization

The concatenated data was mapped to a lower dimensional space by PCA applied to the log-normalized counts filtered for highly variable genes using Scanpy's *highly_variable_genes*. Next, we computed nearest neighbors and conducted Leiden clustering [67] using Scanpy.

Initially, this approach was performed on the control and TeNT datasets separately. This resulted in the identification of 19 clusters in the control data and 22 clusters in the TeNT data (Supplementary Figure 11. 16). For both conditions, equal contribution from both datasets indicated that there was minimal batch effect, as expected since the data was sequenced in a pooled sequencing run. We also performed batch correction using scVI [68] which did not change the contribution of each dataset per cluster. As a result, we continued the analysis using the data that was not batch-corrected with scVI.

Next, we concatenated all four datasets and followed the approach described above. This resulted in the identification of 21 Leiden clusters, which we also refer to as cell types (Supplementary Figure 16A). Each cluster was manually annotated with a cell type based on the expression of previously established marker genes [69]. The cell type annotation was validated by the top 20 differentially expressed genes extracted from each cluster using Scanpy's rank_genes_groups (P values were computed using a t-test and adjusted with the Bonferroni method for multiple testing) (Supplementary Figure 11). Clusters identified as glutamatergic neurons were further broken down into HVC-X- and HVC-RA-projecting glutamatergic neurons using previously established marker genes (data not shown; also see https://github.com/lauraluebbert/TL_2023). We found that reclustering all cells labeled as glutamatergic neurons using the Leiden algorithm did not yield different results and we therefore continued with the initial clusters (data not shown). All results discussed in this paper were confirmed by both jointly and separately clustering the experimental conditions.

Comparative analysis of clusters and conditions

Differentially expressed genes between clusters were identified using Scanpy's *rank_genes_groups* (p values were computed using a t-test and adjusted with the Bonferroni method for multiple testing, and confirmed by comparison to P values generated with Wilcoxon test with Bonferroni correction). In the violin plots, unless otherwise indicated, a star indicates a p value < 0.05 and a fold change > 1.5 difference in mean gene expression between the indicated conditions (p value computed with scipy.stats' (v1.7.0) *ttest_ind* and adjusted with the Bonferroni method for multiple testing).

***In situ* hybridization**

Animals

All of the work described in this study was approved by the California Institute of Technology and Oregon Health & Science University's Institutional Animal Care and Use Committee and is in accordance with NIH guidelines. Zebra finches (Taeniopygia guttata) were obtained from our own breeding colony or purchased from local breeders. Developmental gene expression in HVC in the 20-, 50-, and 75-days post-hatch (dph) male and female zebra finches was assessed as previously described [70]. The sex of birds was determined by plumage and gonadal inspection. Birds were sacrificed by decapitation, bisected in the sagittal plane and flash-frozen in Tissue-Tek OCT (Sakura-Finetek), and frozen in a dry ice/isopropyl alcohol slurry. Brains of TeNT-manipulated finches were

709 coronally blocked anterior to the tectum and flash frozen in Tissue-Tek (Sakura). All brains were
710 sectioned at 10um on a cryostat and mounted onto charged slides (Superfrost Plus, Fisher).
711 In situ hybridization
712 *In situ* hybridization was performed as previously described [71,72]. Briefly, DIG-labeled riboprobes
713 were synthesized from cDNA clones for RGS10 (CK312091) and LOC100231469 (class I
714 histocompatibility antigen, F10 alpha chain; DV951963). Slides containing the core of HVC were
715 hybridized overnight at 65°C. Following high stringency washes, sections were blocked for 30 min
716 and then incubated in an alkaline phosphatase conjugated anti-DIG antibody (1:600, Roche). Slides
717 were then washed and developed overnight in BCIP/NBT chromogen (Perkin Elmer). To minimize
718 experimental confounds between animals, sections for each gene were fixed together in 3%
719 paraformaldehyde, hybridized with the same batch of probe, and incubated in chromogen for the same
720 duration.
721 Sections were imaged under consistent conditions on a Nikon E600 microscope with a Lumina HR
722 camera and imported into ImageJ for analysis. We quantified the expression level of the gene as
723 measured by optical density and the number of cells expressing the gene per unit area, as previously
724 described [70]. Optical density was measured by taking the average pixel intensity of a 300x300 pixel
725 square placed over the center of HVC. This value was normalized to the average background level of
726 the tissue. To quantify the number of labeled cells, we established a threshold of expression that was
727 2.5x the background level. Binary filters (Close-, Open) were applied and the number of particles in
728 the same 300x300 pixel square was quantified.
729 **Histology**
730 After cardiac perfusion with room temperature 3.2% PFA in 1xPBS we let the brains fix for 2-4 hours
731 at room temperature. After each hemisphere of the brain was sectioned sagittally with a vibratome at
732 70-100 µm thickness. The brain slices containing HVC were collected and incubated at 4 C overnight
733 with the primary rabbit anti-GFP (AB3080P, EMD Milipore) (blocked in 10% donkey serum in 0.2%
734 Triton 1xPBS). On the second day, the brains were washed in 0.05% Triton 1xPBS and incubated for
735 2 hours in the dark at room temperature in the secondary goat anti-rabbit 488 (ab150077). Next, the
736 brain slices were washed and mounted in Fluoromount (Sigma). Confocal images were taken with the
737 LSM800.
738
739

Data and Code Availability

Data generated in this study have been deposited in Caltech DATA and can be found at the following DOIs: https://doi.org/10.22002/ednra-nn006 and https://doi.org/10.22002/3ta8v-gj982. Please do not hesitate to contact the authors for data or code requests. The code used for the analysis of the single-cell RNA sequencing data can be found here: https://github.com/lauraluebbert/TL_2023. The code used for the analysis of the chronic electrophysiology data can be found here: https://github.com/jordan-feldman/Torok2023-ephys.

Author contributions

Conceived the ideas of experimental design of the study – ZT, CL
Perform behavioral, single-cell, and electrophysiology experiments/ data collection – ZT
Perform molecular or imaging experiments/ data collection – ZT, LL, SW, AAN, JP (from methods)
Data analysis and interpretation – ZT, LL, JF, AD, WG
Manuscript writing – ZT, CL, AD, AF, LL, LP
Stylistic/grammatical revisions – All authors
Provided revisions to the scientific content of manuscript - All authors
Provided funding – ZT, AF, LP, CL

Acknowledgments

Funding source: R01NS104925A (CL, AF), Chen Graduate Innovator Grant 2019 (ZT)
We thank Jeff Park and the Caltech Sequencing Facility for the library generation.
We thank Daniel Pollak for early chronic electrophysiology advice and Allan Hermann-Pool for advice on the single-cell RNA sequencing experimental pipeline.

Declaration of Interests

The authors declare no competing interests.

References

1. Dehghani, N., Peyrache, A., Telenczuk, B., Le Van Quyen, M., Halgren, E., Cash, S.S., Hatsopoulos, N.G., and Destexhe, A. (2016). Dynamic Balance of Excitation and Inhibition in Human and Monkey Neocortex. Sci. Rep. *6*, 23176.

2. Fritschy, J.-M. (2008). Epilepsy, E/I balance and GABA(A) receptor plasticity. Front. Mol. Neurosci. *1*, 5.

3. Cossart, R., Bernard, C., and Ben-Ari, Y. (2005). Multiple facets of GABAergic neurons and synapses: multiple fates of GABA signalling in epilepsies. Trends Neurosci. *28*, 108–115.

4. Nottebohm, F., Stokes, T.M., and Leonard, C.M. (1976). Central control of song in the canary, Serinus canarius. J. Comp. Neurol. *165*, 457–486.

5. Kozhevnikov, A.A., and Fee, M.S. (2007). Singing-related activity of identified HVC neurons in the zebra finch. J. Neurophysiol. *97*, 4271–4283.

6. Kosche, G., Vallentin, D., and Long, M.A. (2015). Interplay of inhibition and excitation shapes a premotor neural sequence. J. Neurosci. *35*, 1217–1227.

7. Dimidschstein, J., Chen, Q., Tremblay, R., Rogers, S.L., Saldi, G.-A., Guo, L., Xu, Q., Liu, R., Lu, C., Chu, J., et al. (2016). A viral strategy for targeting and manipulating interneurons across vertebrate species. Nat. Neurosci. *19*, 1743–1749.

8. Link, E., Edelmann, L., Chou, J.H., Binz, T., Yamasaki, S., Eisel, U., Baumert, M., Südhof, T.C., Niemann, H., and Jahn, R. (1992). Tetanus toxin action: inhibition of neurotransmitter release linked to synaptobrevin proteolysis. Biochem. Biophys. Res. Commun. *189*, 1017–1023.

9. Vu, E.T., Mazurek, M.E., and Kuo, Y.C. (1994). Identification of a forebrain motor programming network for the learned song of zebra finches. J. Neurosci. *14*, 6924–6934.

10. Yu, A.C., and Margoliash, D. (1996). Temporal hierarchical control of singing in birds. Science *273*, 1871–1875.

11. Glaze, C.M., and Troyer, T.W. (2006). Temporal structure in zebra finch song: implications for motor coding. J. Neurosci. *26*, 991–1005.

12. Wang, B., Torok, Z., Duffy, A., Bell, D., Wongso, S., Velho, T., Fairhall, A., and Lois, C. (2022). Unsupervised Restoration of a Complex Learned Behavior After Large-Scale Neuronal Perturbation. bioRxiv, 2022.09.09.507372. 10.1101/2022.09.09.507372.

13. Thompson, J.A., Wu, W., Bertram, R., and Johnson, F. (2007). Auditory-dependent vocal recovery in adult male zebra finches is facilitated by lesion of a forebrain pathway that includes the basal ganglia. J. Neurosci. *27*, 12308–12320.

14. Simpson, H.B., and Vicario, D.S. (1990). Brain pathways for learned and unlearned vocalizations differ in zebra finches. J. Neurosci. *10*, 1541–1556.

15. Simpson, E. (1988). Function of the MHC. Immunol. Suppl. *1*, 27–30.

16. Elmer, B.M., and McAllister, A.K. (2012). Major histocompatibility complex class I proteins in

808 brain development and plasticity. Trends Neurosci. *35*, 660–670.

809 17. Chacon, M.A., and Boulanger, L.M. (2013). MHC class I protein is expressed by neurons and neural
810 progenitors in mid-gestation mouse brain. Mol. Cell. Neurosci. *52*, 117–127.

811 18. Shatz, C.J. (2009). MHC class I: an unexpected role in neuronal plasticity. Neuron *64*, 40–45.

812 19. Lazarczyk, M.J., Kemmler, J.E., Eyford, B.A., Short, J.A., Varghese, M., Sowa, A., Dickstein, D.R.,
813 Yuk, F.J., Puri, R., Biron, K.E., et al. (2016). Major Histocompatibility Complex class I proteins are
814 critical for maintaining neuronal structural complexity in the aging brain. Sci. Rep. *6*, 26199.

815 20. Prabowo, A.S., Iyer, A.M., Anink, J.J., Spliet, W.G.M., van Rijen, P.C., and Aronica, E. (2013).
816 Differential expression of major histocompatibility complex class I in developmental glioneuronal
817 lesions. J. Neuroinflammation *10*, 12.

818 21. Lenz, K.M., and Nelson, L.H. (2018). Microglia and Beyond: Innate Immune Cells As Regulators of
819 Brain Development and Behavioral Function. Front. Immunol. *9*, 698.

820 22. Thion, M.S., Ginhoux, F., and Garel, S. (2018). Microglia and early brain development: An intimate
821 journey. Science *362*, 185–189.

822 23. Parkhurst, C.N., Yang, G., Ninan, I., Savas, J.N., Yates, J.R., 3rd, Lafaille, J.J., Hempstead, B.L.,
823 Littman, D.R., and Gan, W.-B. (2013). Microglia promote learning-dependent synapse formation
824 through brain-derived neurotrophic factor. Cell *155*, 1596–1609.

825 24. Lombardino, A.J., and Nottebohm, F. (2000). Age at deafening affects the stability of learned song
826 in adult male zebra finches. J. Neurosci. *20*, 5054–5064.

827 25. Nordeen, K.W., and Nordeen, E.J. (1992). Auditory feedback is necessary for the maintenance of
828 stereotyped song in adult zebra finches. Behav. Neural Biol. *57*, 58–66.

829 26. Brainard, M.S., and Doupe, A.J. (2001). Postlearning consolidation of birdsong: stabilizing effects of
830 age and anterior forebrain lesions. J. Neurosci. *21*, 2501–2517.

831 27. Eyo, U.B., Peng, J., Murugan, M., Mo, M., Lalani, A., Xie, P., Xu, P., Margolis, D.J., and Wu, L.-J.
832 (2016). Regulation of physical microglia–neuron interactions by fractalkine signaling after status
833 epilepticus. eNeuro *3*, ENEURO.0209–0216.2016.

834 28. Kinoshita, S., and Koyama, R. (2021). Pro- and anti-epileptic roles of microglia. Neural
835 Regeneration Res. *16*, 1369–1371.

836 29. Markowitz, J.E., Liberti, W.A., 3rd, Guitchounts, G., Velho, T., Lois, C., and Gardner, T.J. (2015).
837 Mesoscopic patterns of neural activity support songbird cortical sequences. PLoS Biol. *13*,
838 e1002158.

839 30. Brown, D.E., 2nd, Chavez, J.I., Nguyen, D.H., Kadwory, A., Voytek, B., Arneodo, E.M., Gentner,
840 T.Q., and Gilja, V. (2021). Local field potentials in a pre-motor region predict learned vocal
841 sequences. PLoS Comput. Biol. *17*, e1008100.

842 31. Buzsáki, G., Anastassiou, C.A., and Koch, C. (2012). The origin of extracellular fields and currents
843 — EEG, ECoG, LFP and spikes. Nat. Rev. Neurosci. *13*, 407–420.

844 32. Crandall, S.R., Adam, M., Kinnischtzke, A.K., and Nick, T.A. (2007). HVC neural sleep activity

increases with development and parallels nightly changes in song behavior. J. Neurophysiol. *98*, 232–240.

33. Dave, A.S., and Margoliash, D. (2000). Song replay during sleep and computational rules for sensorimotor vocal learning. Science *290*, 812–816.

34. Elmaleh, M., Kranz, D., Asensio, A.C., Moll, F.W., and Long, M.A. (2021). Sleep replay reveals premotor circuit structure for a skilled behavior. Neuron *109*, 3851–3861.e4.

35. Hahnloser, R.H.R., Kozhevnikov, A.A., and Fee, M.S. (2006). Sleep-related neural activity in a premotor and a basal-ganglia pathway of the songbird. J. Neurophysiol. *96*, 794–812.

36. Shank, S.S., and Margoliash, D. (2009). Sleep and sensorimotor integration during early vocal learning in a songbird. Nature *458*, 73–77.

37. Jun, J.J., Steinmetz, N.A., Siegle, J.H., Denman, D.J., Bauza, M., Barbarits, B., Lee, A.K., Anastassiou, C.A., Andrei, A., Aydın, Ç., et al. (2017). Fully integrated silicon probes for high-density recording of neural activity. Nature *551*, 232–236.

38. Steinmetz, N.A., Koch, C., Harris, K.D., and Carandini, M. (2018). Challenges and opportunities for large-scale electrophysiology with Neuropixels probes. Curr. Opin. Neurobiol. *50*, 92–100.

39. Fisher, R.S., Scharfman, H.E., and deCurtis, M. (2014). How can we identify ictal and interictal abnormal activity? Adv. Exp. Med. Biol. *813*, 3–23.

40. Spiro, J.E., Dalva, M.B., and Mooney, R. (1999). Long-range inhibition within the zebra finch song nucleus RA can coordinate the firing of multiple projection neurons. J. Neurophysiol. *81*, 3007–3020.

41. Grossmann, A., and Morlet, J. (1984). Decomposition of Hardy Functions into Square Integrable Wavelets of Constant Shape. SIAM J. Math. Anal. *15*, 723–736.

42. Lubenov, E.V., and Siapas, A.G. (2009). Hippocampal theta oscillations are travelling waves. Nature *459*, 534–539.

43. Brainard, M.S., and Doupe, A.J. (2002). What songbirds teach us about learning. Nature *417*, 351–358.

44. Liu, W.-C., Gardner, T.J., and Nottebohm, F. (2004). Juvenile zebra finches can use multiple strategies to learn the same song. Proc. Natl. Acad. Sci. U. S. A. *101*, 18177–18182.

45. Olveczky, B.P., Andalman, A.S., and Fee, M.S. (2005). Vocal experimentation in the juvenile songbird requires a basal ganglia circuit. PLoS Biol. *3*, e153.

46. Mooney, R. (2009). Neurobiology of song learning. Curr. Opin. Neurobiol. *19*, 654–660.

47. Price, P.H. (1979). Developmental determinants of structure in zebra finch song. J. Comp. Physiol. Psychol. *93*, 260–277.

48. Warren, T.L., Tumer, E.C., Charlesworth, J.D., and Brainard, M.S. (2011). Mechanisms and time course of vocal learning and consolidation in the adult songbird. J. Neurophysiol. *106*, 1806–1821.

49. Kittelberger, J.M., and Mooney, R. (1999). Lesions of an avian forebrain nucleus that disrupt song

881 development alter synaptic connectivity and transmission in the vocal premotor pathway. J.
882 Neurosci. *19*, 9385–9398.

883 50. Kao, M.H., Doupe, A.J., and Brainard, M.S. (2005). Contributions of an avian basal ganglia–
884 forebrain circuit to real-time modulation of song. Nature *433*, 638–643.

885 51. Morrison, R.G., and Nottebohm, F. (1993). Role of a telencephalic nucleus in the delayed song
886 learning of socially isolated zebra finches. J. Neurobiol. *24*, 1045–1064.

887 52. Williams, H., and Mehta, N. (1999). Changes in adult zebra finch song require a forebrain nucleus
888 that is not necessary for song production. J. Neurobiol. *39*, 14–28.

889 53. Ali, F., Otchy, T.M., Pehlevan, C., Fantana, A.L., Burak, Y., and Ölveczky, B.P. (2013). The basal
890 ganglia is necessary for learning spectral, but not temporal, features of birdsong. Neuron *80*, 494–
891 506.

892 54. Li, Q., and Barres, B.A. (2018). Microglia and macrophages in brain homeostasis and disease. Nat.
893 Rev. Immunol. *18*, 225–242.

894 55. Mooney, R. (2009). Neural mechanisms for learned birdsong. Learn. Mem. *16*, 655–669.

895 56. Brainard, M.S., and Doupe, A.J. (2000). Interruption of a basal ganglia–forebrain circuit prevents
896 plasticity of learned vocalizations. Nature *404*, 762–766.

897 57. Tchernichovski, O., Nottebohm, F., Ho, C.E., Pesaran, B., and Mitra, P.P. (2000). A procedure for
898 an automated measurement of song similarity. Anim. Behav. *59*, 1167–1176.

899 58. Goffinet, J., Brudner, S., Mooney, R., and Pearson, J. (2021). Low-dimensional learned feature
900 spaces quantify individual and group differences in vocal repertoires. Elife *10*. 10.7554/eLife.67855.

901 59. Sainburg, T., Thielk, M., and Gentner, T.Q. (2020). Finding, visualizing, and quantifying latent
902 structure across diverse animal vocal repertoires. PLoS Comput. Biol. *16*, e1008228.

903 60. Yeganegi, H., Luksch, H., and Ondracek, J.M. (2019). Hippocampal-like network dynamics underlie
904 avian sharp wave-ripples. bioRxiv, 825075. 10.1101/825075.

905 61. Shan, K.Q., Lubenov, E.V., and Siapas, A.G. (2017). Model-based spike sorting with a mixture of
906 drifting t-distributions. J. Neurosci. Methods *288*, 82–98.

907 62. Pachitariu, M., Steinmetz, N., Kadir, S., Carandini, M., and Harris, K.D. (2016). Kilosort: realtime
908 spike-sorting for extracellular electrophysiology with hundreds of channels. bioRxiv, 061481.
909 10.1101/061481.

910 63. Pool, A.-H., Wang, T., Stafford, D.A., Chance, R.K., Lee, S., Ngai, J., and Oka, Y. (2020). The
911 cellular basis of distinct thirst modalities. Nature *588*, 112–117.

912 64. Melsted, P., Sina Booeshaghi, A., Gao, F., Beltrame, E., Lu, L., Hjorleifsson, K.E., Gehring, J., and
913 Pachter, L. (2019). Modular and efficient pre-processing of single-cell RNA-seq. bioRxiv, 673285.
914 10.1101/673285.

915 65. Wolf, F.A., Angerer, P., and Theis, F.J. (2018). SCANPY: large-scale single-cell gene expression
916 data analysis. Genome Biol. *19*, 15.

66. Luebbert, L., and Pachter, L. (2023). Efficient querying of genomic reference databases with gget. Bioinformatics *39*. 10.1093/bioinformatics/btac836.

67. Traag, V.A., Waltman, L., and van Eck, N.J. (2019). From Louvain to Leiden: guaranteeing well-connected communities. Sci. Rep. *9*, 5233.

68. Lopez, R., Regier, J., Cole, M.B., Jordan, M.I., and Yosef, N. (2018). Deep generative modeling for single-cell transcriptomics. Nat. Methods *15*, 1053–1058.

69. Colquitt, B.M., Merullo, D.P., Konopka, G., Roberts, T.F., and Brainard, M.S. (2021). Cellular transcriptomics reveals evolutionary identities of songbird vocal circuits. Science *371*. 10.1126/science.abd9704.

70. Zemel, B.M., Nevue, A.A., Dagostin, A., Lovell, P.V., Mello, C.V., and von Gersdorff, H. (2021). Resurgent Na+ currents promote ultrafast spiking in projection neurons that drive fine motor control. Nat. Commun. *12*, 6762.

71. Carleton, J.B., Lovell, P.V., McHugh, A., Marzulla, T., Horback, K.L., and Mello, C.V. (2014). An optimized protocol for high-throughput in situ hybridization of zebra finch brain. Cold Spring Harb. Protoc. *2014*, 1249–1258.

72. Nevue, A.A., Lovell, P.V., Wirthlin, M., and Mello, C.V. (2020). Molecular specializations of deep cortical layer analogs in songbirds. Sci. Rep. *10*, 18767.

Supplementary Figures

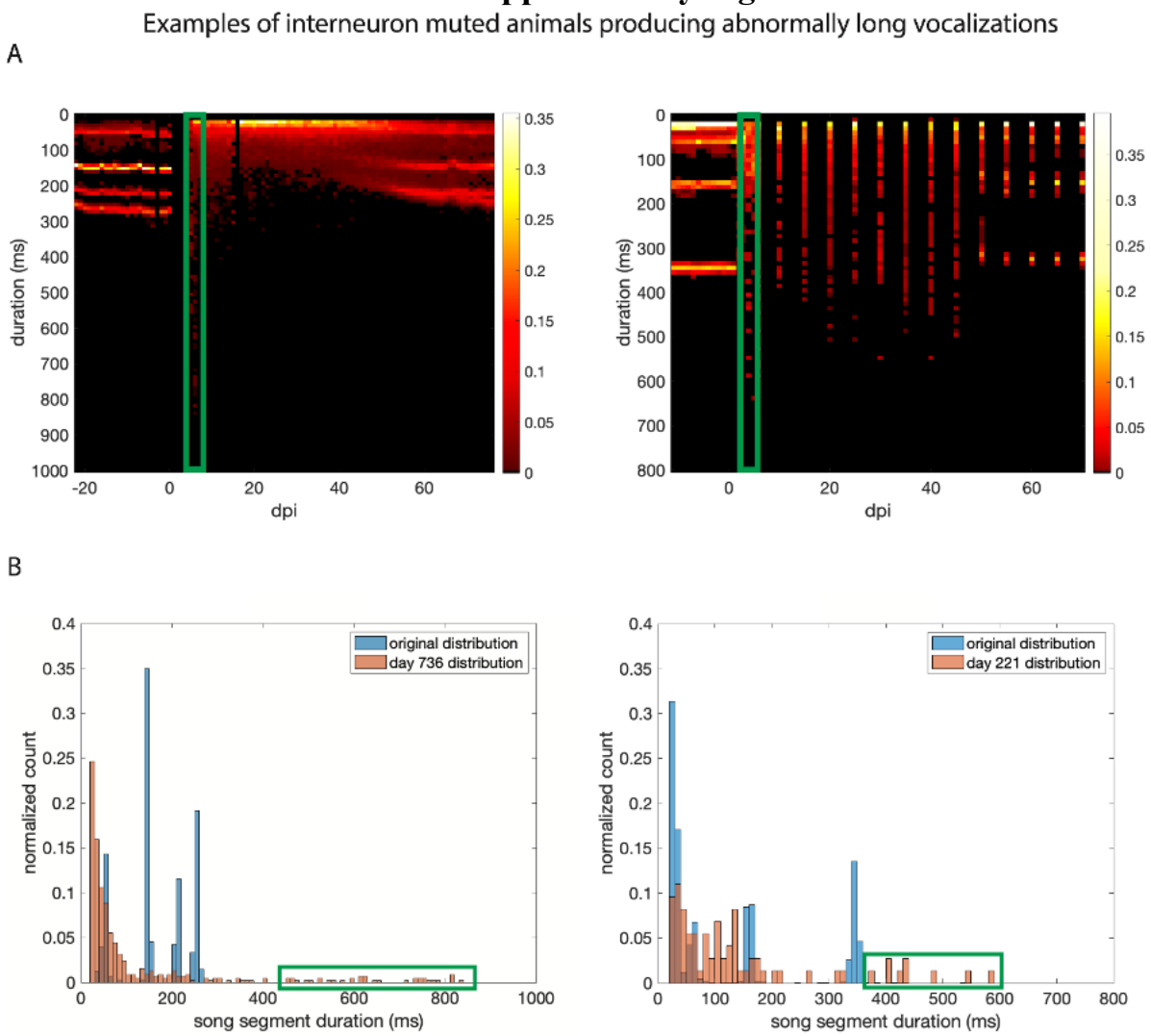

Supplementary Figure 1: *Examples of abnormally long syllable lengths after injection of interneuron muting virus in two animals.* ***A*** *Syllable length durations for the length of song degradation and recovery. The Y axis depicts the length of the syllables in milliseconds plotted over days post-injection (dpi) of either TeNT virus. TeNT-treated animals displayed a short period during which some vocalizations were of length not observed in normal animals and eventually became highly variable and shorter (shifts to shorter length sounds). The green rectangle highlights the day post-injection portrayed in B for each animal.* ***B*** *Histogram of syllable durations (blue trace is before injection of virus, orange trace is after injection of virus). The green rectangle highlights vocalizations of abnormal length.*

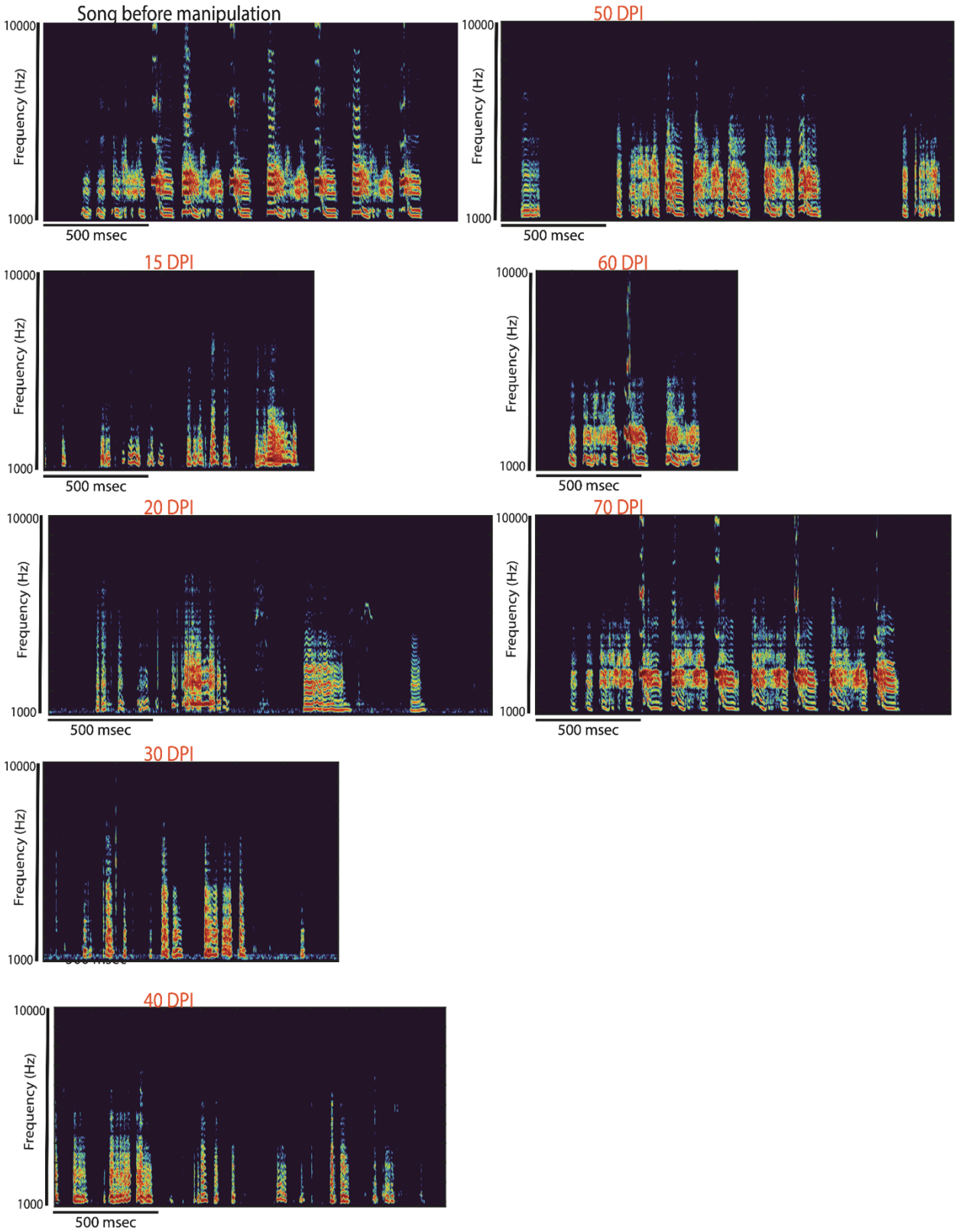

953 *Figure legend on next page.*

954 ***Supplementary Figure 2:*** *Example spectrograms of a TeNT-treated animal (B138) during song degradation*
955 *and recovery. Vocalizations between 15 dpi and 30 dpi were much shorter than the first long syllables shown*
956 *in Figure 1 A at 5 dpi.*
957
958
959
960
961
962

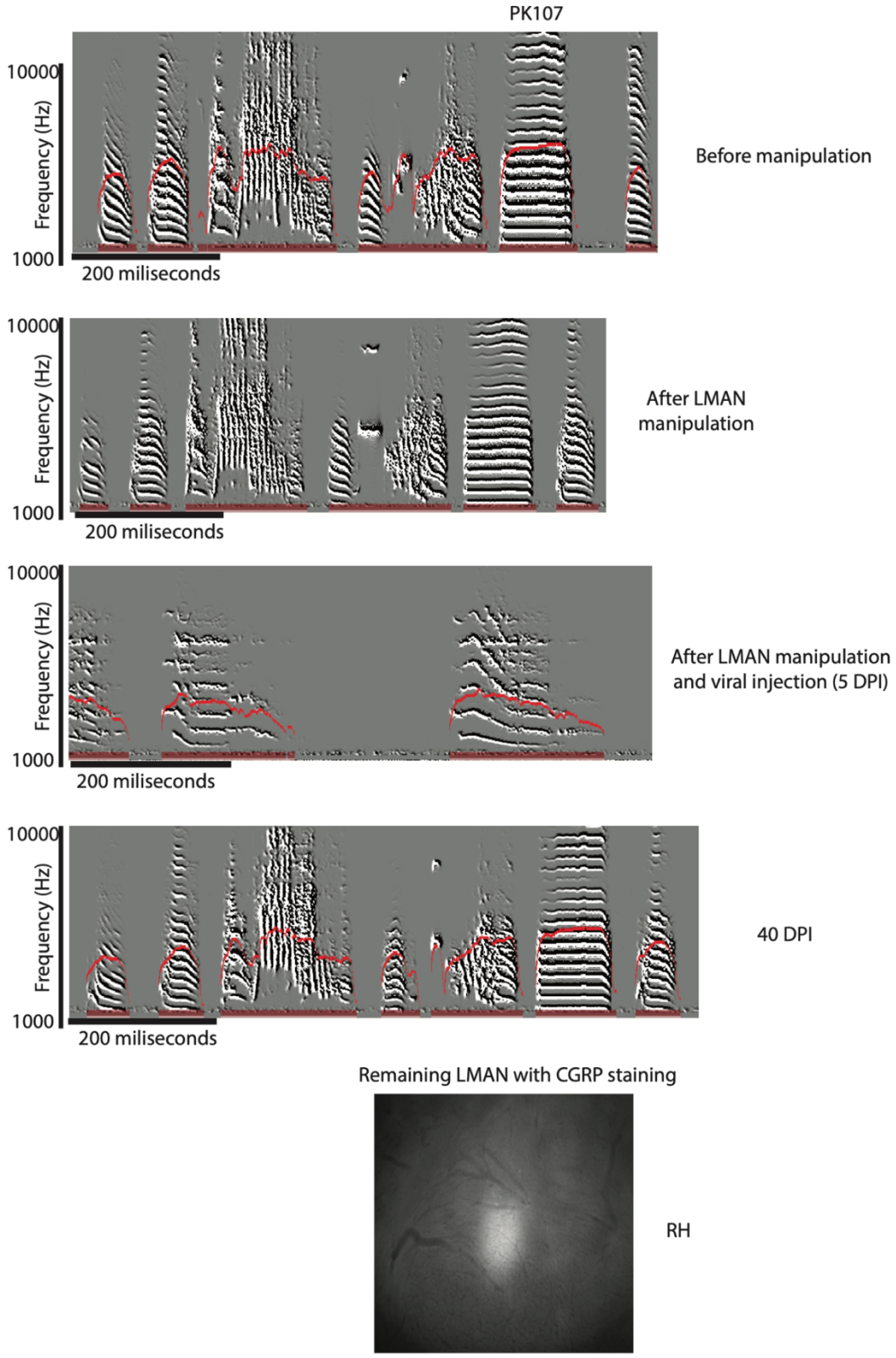

963 *Figure legend on next page.*
964

965 ***Supplementary Figure 3:*** *Song degradation and recovery after chronic removal of inhibition in an animal*
966 *without LMAN. Spectrograms are showing the song of the animal before and after LMAN lesion at 5 and 40*
967 *days post viral injection (dpi). The histology image shows the amount of LMAN left (based on CGRP staining)*
968 *in the right hemisphere (RH).*
969

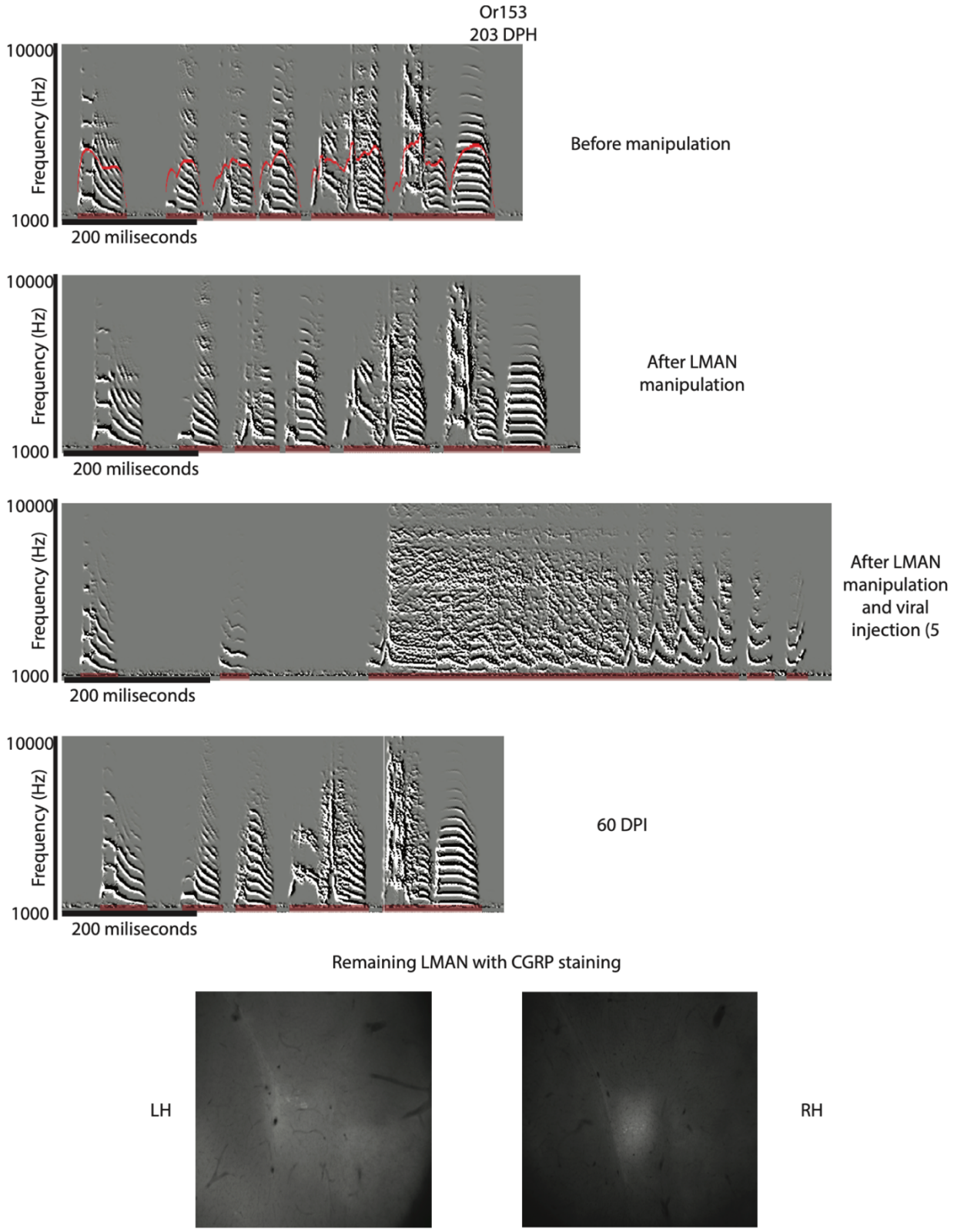

Figure legend on next page.

Supplementary Figure 4: *Song degradation and recovery after chronic removal of inhibition in an animal without LMAN. Spectrograms are showing the song of the animal before and after LMAN lesion at 5 and 60 days post viral injection (dpi). The histology images indicate the amount of LMAN left (based on CGRP staining) in the left (LH) and right (RH) hemispheres.*

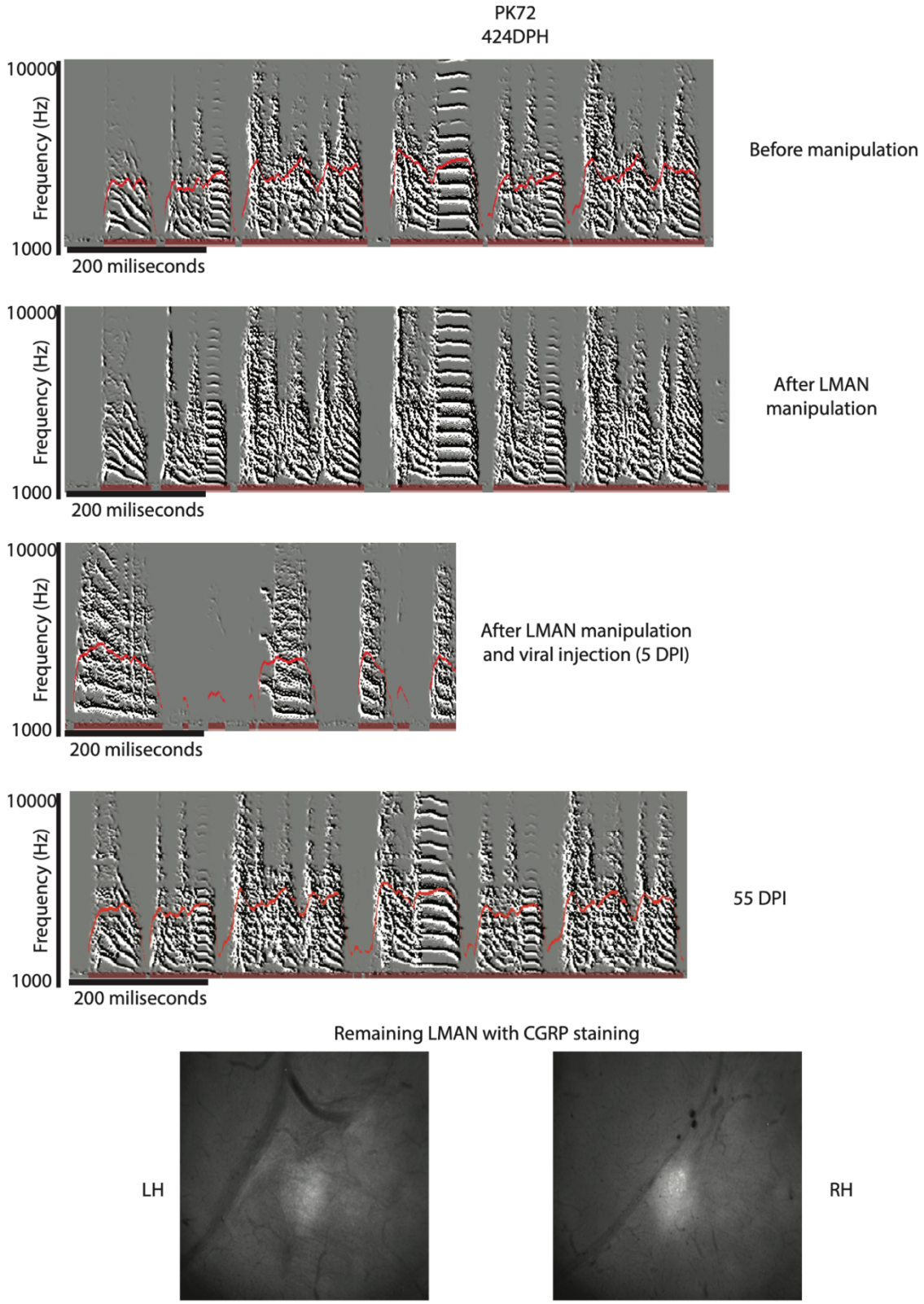

Figure legend on next page.

980 ***Supplementary Figure 5:*** *Song degradation and recovery after chronic removal of inhibition in an animal*
981 *without LMAN. Spectrograms are showing the song of the animal before and after LMAN lesion at 5 and 55*
982 *days after viral injection (dpi). The histology images indicate the amount of LMAN left (based on CGRP*
983 *staining) in the left (LH) and right (RH) hemispheres.*
984

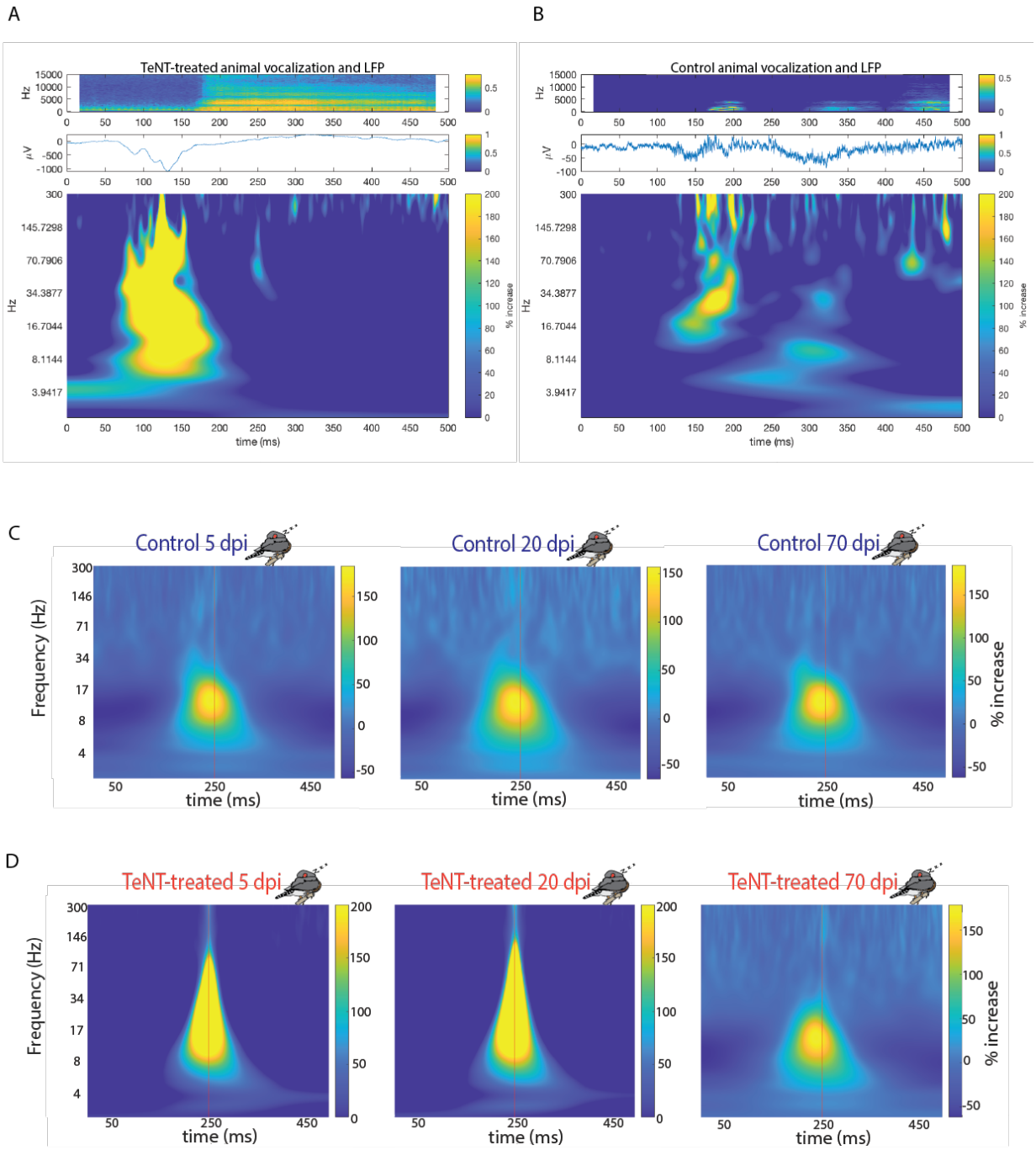

985
986 *Figure legend on next page.*
987

988 ***Supplementary Figure 6:*** *Example electrophysiology traces averaged over 5 instances of normal or 5 instances*
989 *of degraded vocalizations and averages of sleep voltage deflections.* ***A*** *Averaged spectrogram of degraded*
990 *vocalization (n=5) 5 days post-electrode-implantation in a chronically recorded TeNT-treated animal. The plot*
991 *below the spectrogram shows the raw averaged trace of extracellular recording. Below the raw trace is the*
992 *averaged continuous wavelet transform of the local field potentials (LFP, 1-300Hz). The plots show a large*
993 *deflection event (similar to those seen during lights-off in Figures 2 and 3) right before the onset of the*
994 *vocalization in the TeNT-treated animal.* ***B*** *Averaged song spectrogram (n=5) 5 days post-electrode-*
995 *implantation from a chronically recorded control animal. The plot below the spectrogram shows the raw*
996 *averaged trace of extracellular recordings. Below the raw trace is the averaged continuous wavelet transform*
997 *of the local field potentials (LFP, 1-300 Hz). The averaged control song shows more and smaller amplitude*
998 *deflections mostly during the vocalization compared to the TeNT-treated vocalization.* ***C-D*** *Spectral*
999 *decomposition of local field potentials (LFPs) of the averaged deflections during night time at 5, 20, and 60*
1000 *dpi in one control (C) and one TeNT-treated animal (D). The vertical red line depicts the trough of the raw*
1001 *deflection trace. The % increase is the relative increase compared to non-deflection events in the same*
1002 *recording timeframe of the same animal (Methods). Deflections of TeNT-treated animals in the 15-30 Hz range*
1003 *were approx. 27 times larger than those in control animals at 5 dpi. These differences are statistically*
1004 *significant between control and TeNT-treated groups, but not within the control group (p=0.7631 between*
1005 *controls, $p<10^{-35}$ between all other pairs). The deflections across all animals and frequencies become more*
1006 *similar by 60 dpi (15-30 Hz: p=0.1371 between controls, $p<10^{-6}$ between all other pairs; 30-70 Hz: p=0.7493*
1007 *between controls, $p<10^{-2}$ between all other pairs). For details on statistics see Methods.*

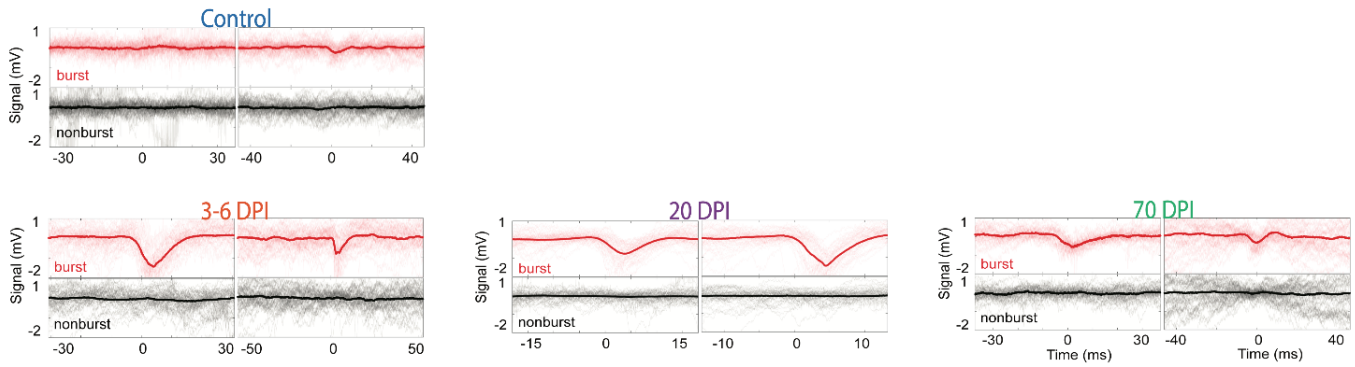

1008 ***Supplementary Figure 7:*** *Example traces of raw deflections in the acute Neuropixel recordings during lights-*
1009 *off periods.* *Control animals barely showed any visible deflection events, while TeNT-treated animals (example*
1010 *traces shown at 3-6, 20, and 70 dpi) displayed large amplitude voltage deflection events.*
1011

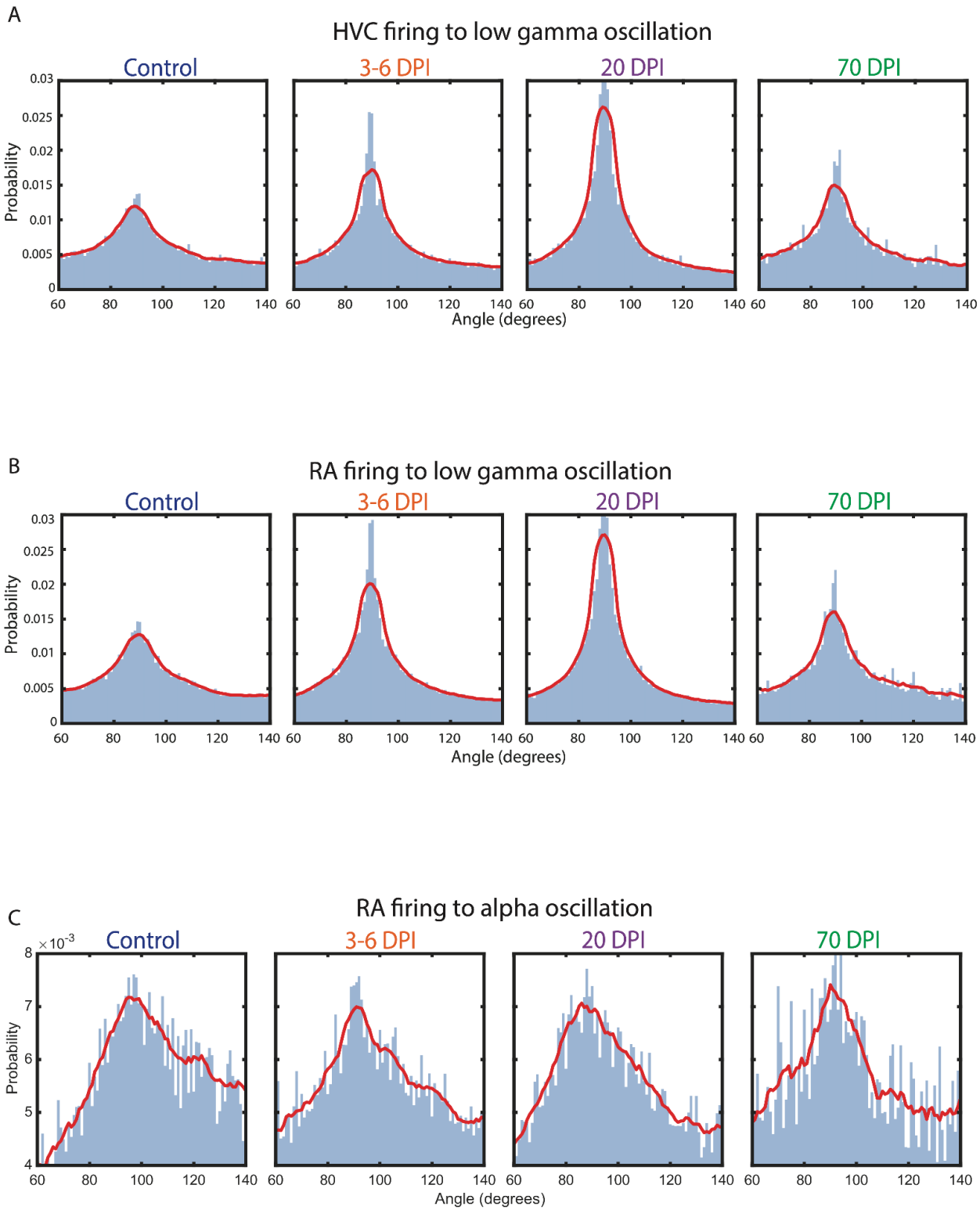

Figure legend on next page.

Supplementary Figure 8: *Relationship between alpha or gamma oscillations during lights-off voltage deflection events and local neuronal firing in HVC and RA from the acute NPIX recordings* ***A*** *The normalized probability distribution of neurons locally within HVC fire during a specific phase (angle) of the gamma (30-40 Hz) oscillations extracted from the LFP signal of the averaged deflection events at 3-6 dpi (n=4 animals), 20 dpi (n=4 animals), 70 dpi (n =2 animals that recovered their song by then). There was a slight change in local neuronal firing to the angle and locking precision to gamma oscillations that resembled control by 70 dpi.* ***B*** *Normalized probability distribution of neurons locally within RA fire during a specific phase (angle) of the alpha (1-10 Hz) oscillations in HVC extracted from the LFP signal of the averaged deflection events at 3-6 dpi, 20, 70 dpi. No change in RA spontaneous neuronal firing to alpha oscillations in HVC during the deflection events over the course of the manipulation.* ***C*** *Normalized probability distribution of neurons locally within RA fire during a specific phase (angle) of the gamma (30-40 Hz) oscillations in HVC extracted from the LFP signal of the averaged deflection events at 3-6, 20, and 70 dpi. We observed no change in RA spontaneous neuronal firing to the gamma oscillations in HVC during the deflection events over the course of the manipulation.*

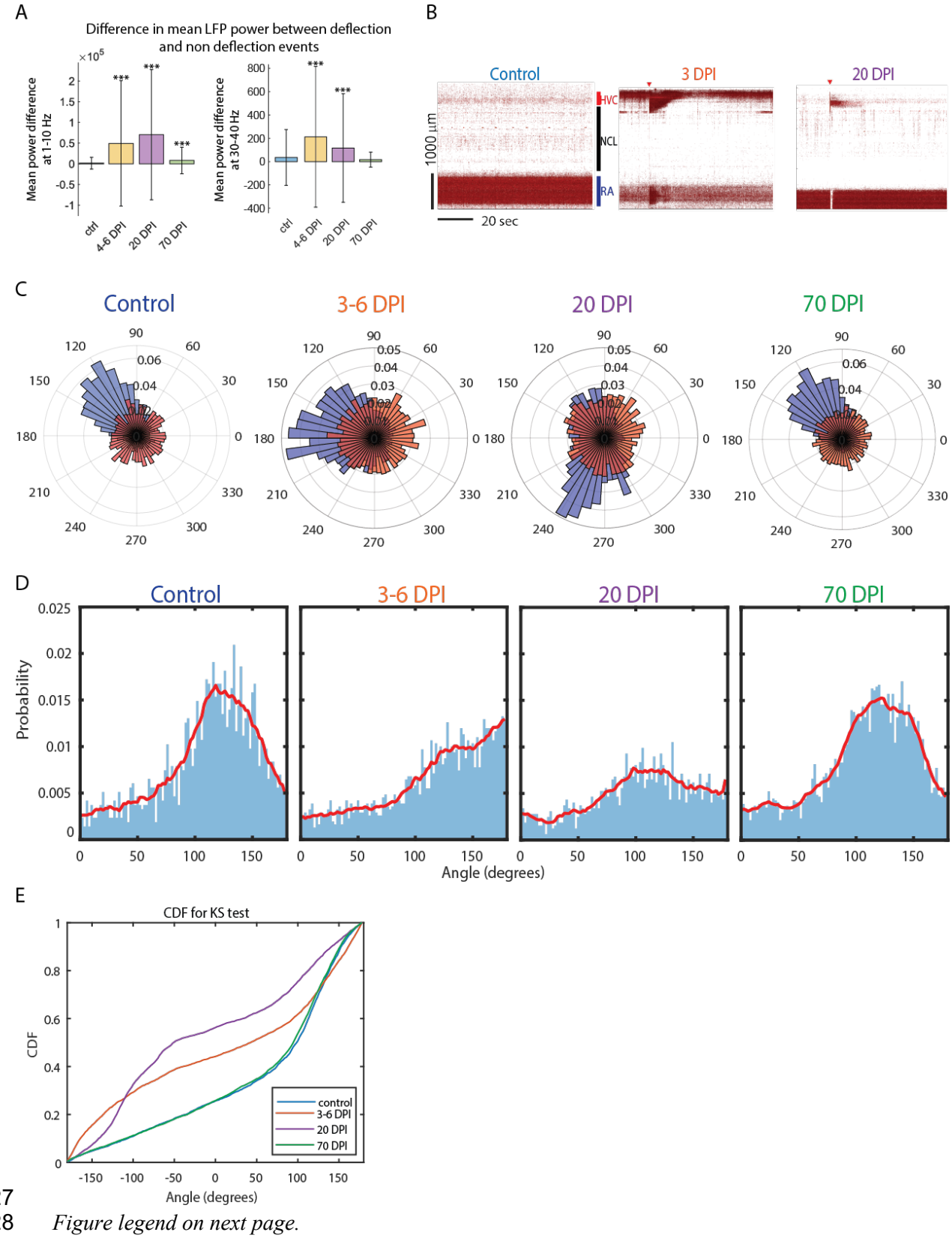

Figure legend on next page.

Supplementary Figure 9: *Quantification of the angle relationship between alpha (1-10 Hz) and gamma (30-40 Hz) frequencies during deflection events in control and TeNT-treated animals during acute head-fixed recordings.* ***A****: The average difference in power (at alpha, 1-10 Hz, and low gamma 30-40 Hz frequency ranges) between voltage deflection and non-deflection events in control, 3-6, 20, 70 dpi. The power content in the alpha range increased in a statistically significant way (Wilcoxon, rank sum test) between control and 3-6 (p=2.9*10^-36), 20 (p=8.6*10^-167), 70 (p=5.4*10^-4) dpi animals. However, the increase in power between control and 3-6 (p=2.2*10^-37), 20 (p=6.3*10^-27) dpi is statistically significant but returns to control level by 70 (p=0.37) dpi. The stars above the bar plots (*) indicate statistical significance (* : p < 0.005, ** : p< 0.01, *** : p < 0.001).* ***B*** *Examples of neuronal activity in a control animal, TeNT-treated animals at 3 and 20 dpi. The red arrows highlight the "superbursts" or extreme firing levels within HVC and RA which we observed in 3 animals (two animals at 3-4 dpi and one at 20 dpi) in a total of seven instances.****C****: The polar histograms of the angle of the alpha oscillations (1-10Hz) at the maximum amplitude of the gamma oscillation (30-40 Hz) during deflection events. The red distribution represents a randomly shuffled dataset, while the blue is the true distribution of angles in control (n=3), and TeNT-treated animals at 3-6 dpi (n=4), 20 dpi (n=4) and 70 dpi (n=4) during deflection events.* ***D****: Relationship of alpha and low gamma oscillations during deflection events in control (n=3), 3-6 (n=4), 20 (n=4), and 70 (n=2 animals) dpi animals (over animals and conditions). The probability distribution of a specific angle of the low-frequency oscillation at the maximum amplitude of the gamma oscillation.* ***E****: The results of the Kolgomorov-Smirnov test on the cumulative density function (CDF) to assess if the change in probability distribution shown in C is statistically significant from control distributions at 3-6, 20, and 70 dpi. The purple (20 dpi) and orange (3-7 dpi) distributions differ significantly from the blue control and the 70 dpi green distributions. The 70 dpi population is not significantly different from the control group.*

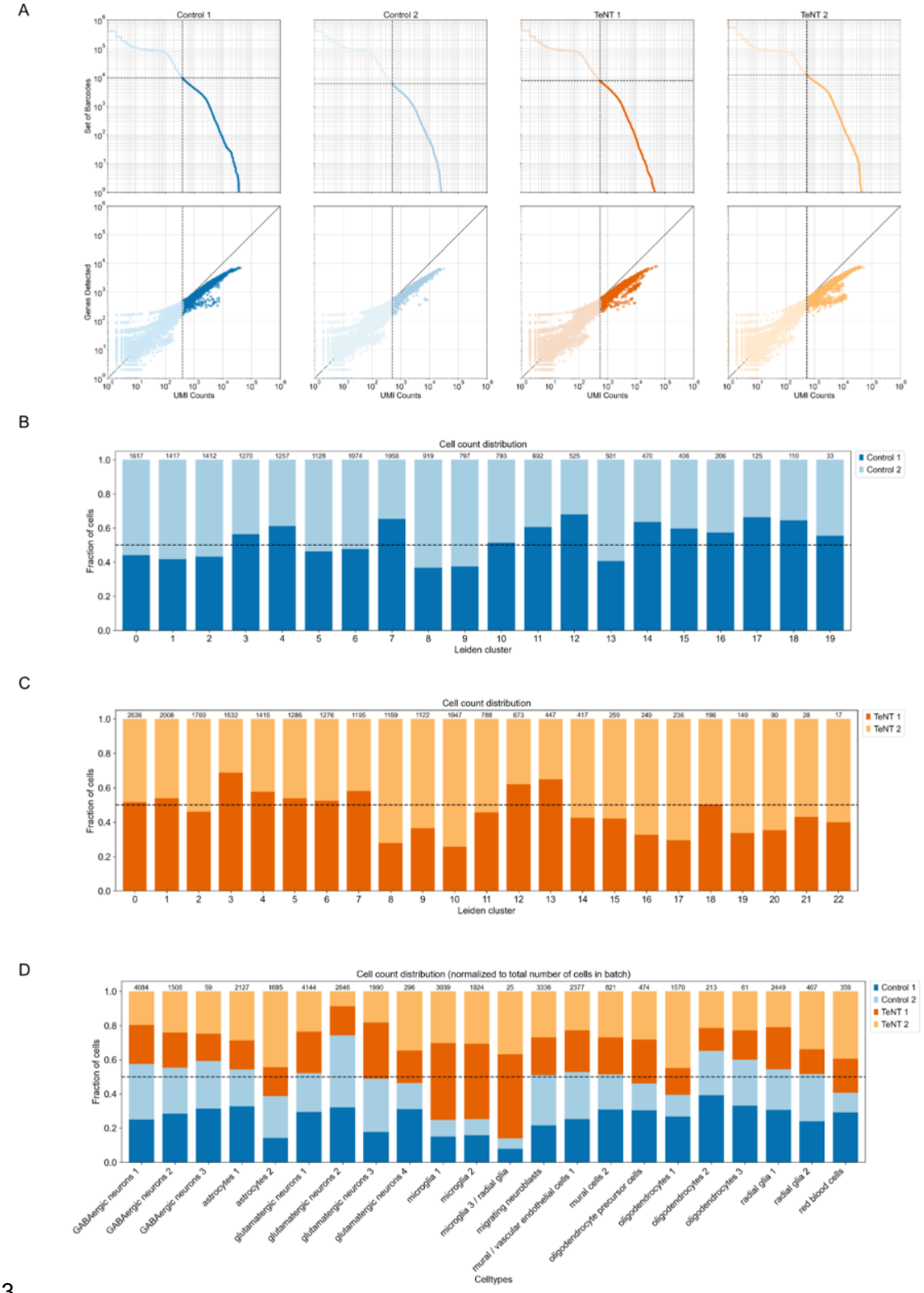

Figure legend on next page.

Supplementary Figure 10: *Quality control of the single-cell RNA sequencing HVC datasets from control and TeTN-treated animals at 25 days post-injection (dpi).* ***A*** *"Knee plots" showing the set of barcodes (top row)*

and number of genes detected (bottom row) over UMI counts. The dashed lines depict the quality filtering cutoff. ***B-C*** *Barplot depicting the fraction of cells from each replicate per cluster for control (B) and TeNT (C), normalized (by dividing) to the total number of cells in each replicate. Control and TeNT datasets were clustered separately using the Leiden algorithm. The equal distribution of replicates across the clusters suggests that technical effects do not dominate the clusters. Thus, we did not perform batch correction. The numbers on top of the bars indicate the total number of cells in each cluster.* ***D*** *Barplot depicting the fraction of cells from each dataset in the cell type clusters obtained after jointly clustering the control and TeNT datasets. The numbers on top of the bars indicate the total number of cells in each cluster.*

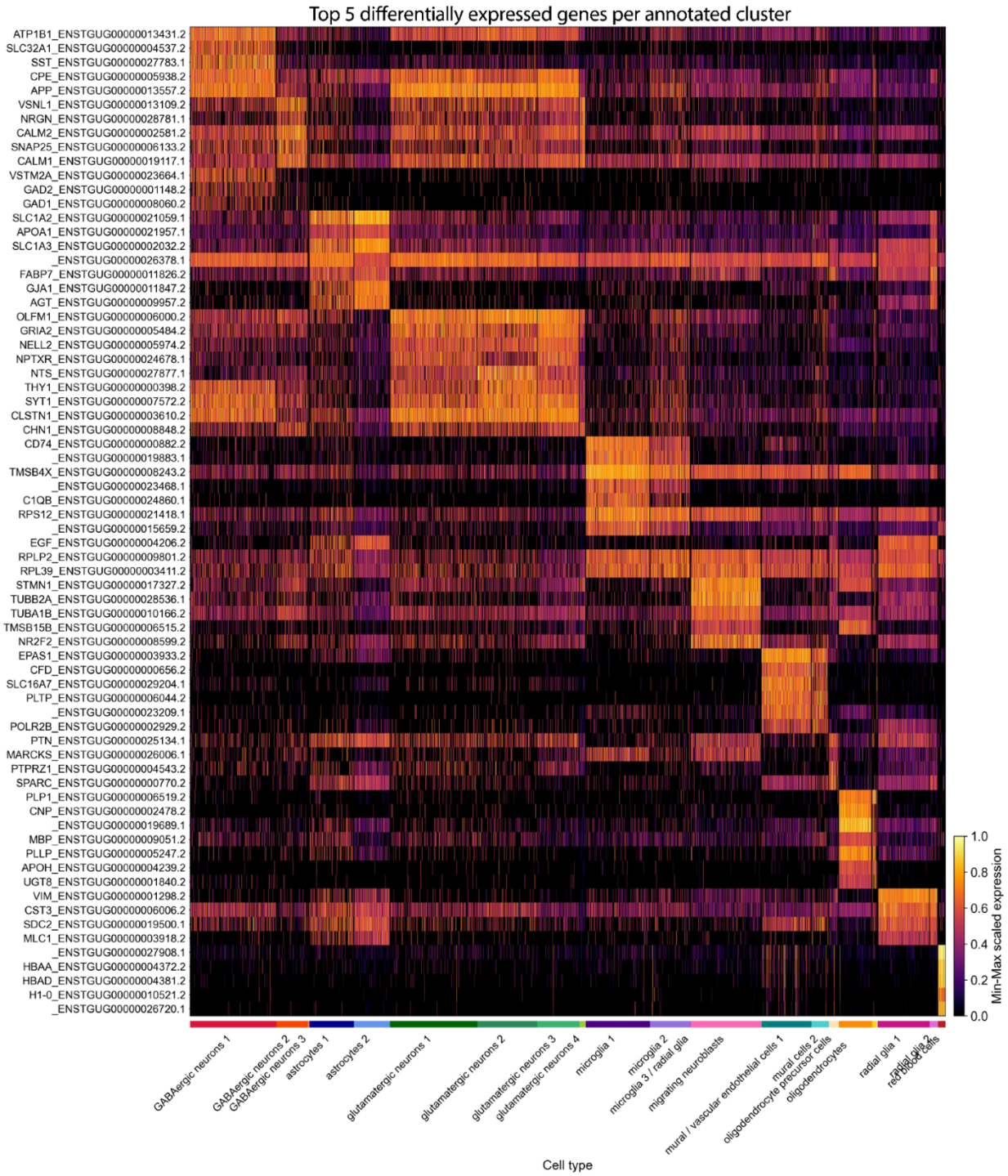

Supplementary Figure 11: *Heatmap of top 5 differentially expressed genes per annotated cell type/cluster obtained by single-cell RNA sequencing of HVC from control and TeNT-treated birds at 25 dpi. Differentially expressed genes between clusters were identified using Scanpy's rank_genes_groups (p values were computed using a t-test and were adjusted with the Bonferroni method for multiple testing. They were then confirmed by comparison to p values generated with the nonparametric Wilcoxon test with Bonferroni correction). The heatmap depicts the min-max scaled expression for each gene.*

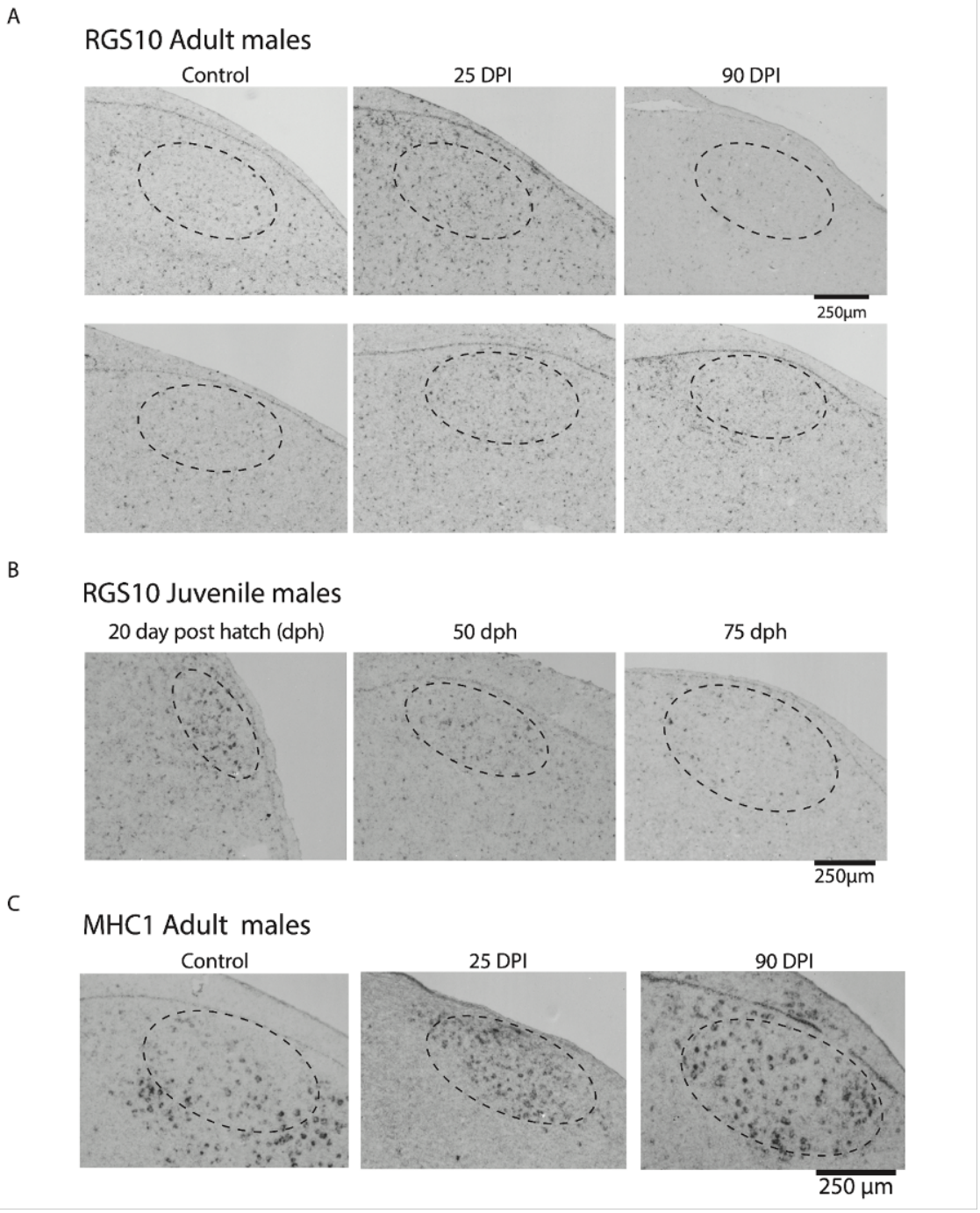

Supplementary Figure 12: *In situ hybridization of microglia marker gene RGS10 in adult male control, TeNT-treated and juvenile male HVC & MHC1 gene in adult male control and TeNT-treated HVC.* ***A*** *Histological sections of HVC (in control and TeNT-treated animals at 25 and 90 dpi) after in situ hybridization of RNA probes for RGS10 (a gene marker for microglia).* ***B*** *Histological sections of HVC in naive juvenile males (at 20, 50, and 75 days post-hatching (dph)) after in situ hybridization of RNA probes for RGS10.* ***C*** *Histological sections of HVC (from control and TeNT-treated animals at 25 and 90 dpi) after in situ hybridization of RNA probes for MHC1. Black/darker dots indicate enzyme reactions resulting in successful probe localization and suggest target gene expression.*

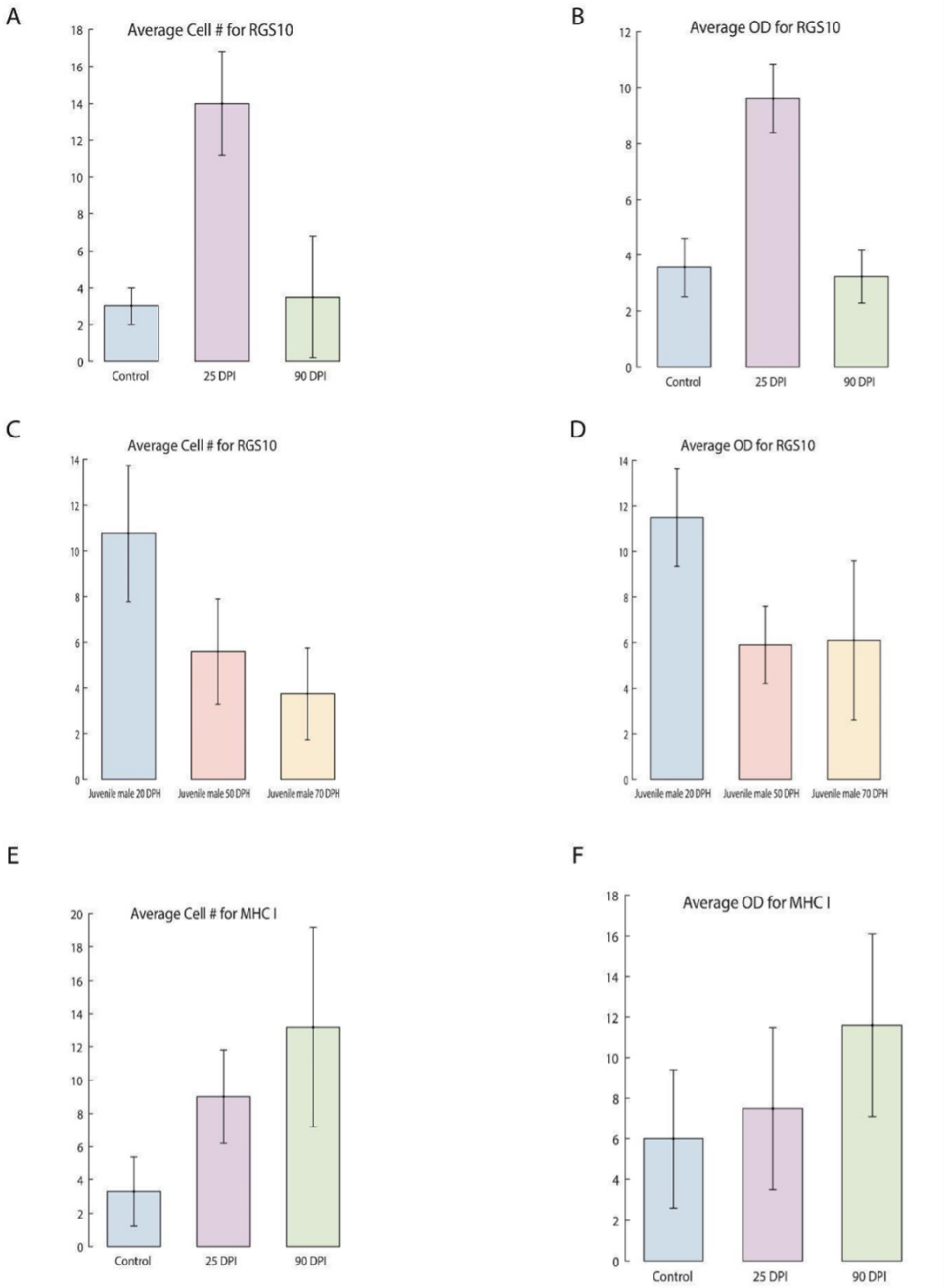

Supplementary Figure 13: *Quantification of the in situ hybridization against microglia marker gene RGS10 in adult male control, TeNT-treated and juvenile male HVC; and MHC1 in adult male control, TeNT-treated animals.* ***A-B*** *Quantification of the in situ hybridization for RGS10 between control (n=4 animals) and TeNT-treated animals at 25 dpi (n=4) and 90 dpi (n=4).* ***C-D*** *Quantification of the in situ hybridization for RGS10 between juvenile males at 20, 50, and 70 days post-hatching (dph) (n=4).* ***E-F*** *Quantification of the in situ hybridization for MHC1 between control (n=4) and TeNT-treated animals at 25 (n=4) and 90 dpi (n=4). Error bars represent standard deviation.*

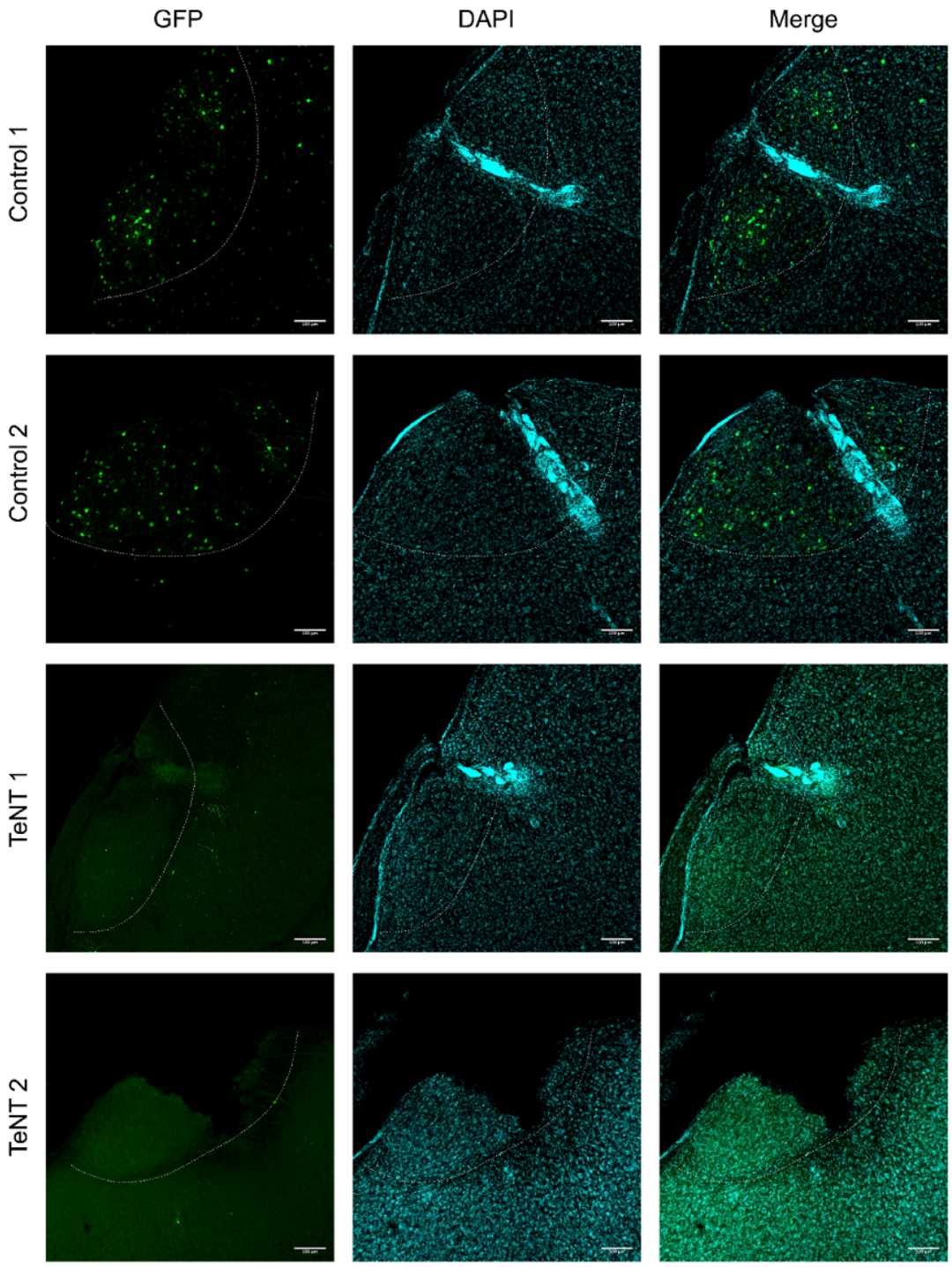

Supplementary Figure 14: *Histology of electrode array location in HVC in the chronically implanted animals. The white dotted line outlines HVC. Some sections display missing tissue due to the removal of the electrodes after perfusion of the animals. The stronger cyan signal indicates glial scar formation around the electrode array, which provides an approximation of the location of the electrodes. Electrodes located closer to the bottom of HVC close to the shelf were not used for analysis.*

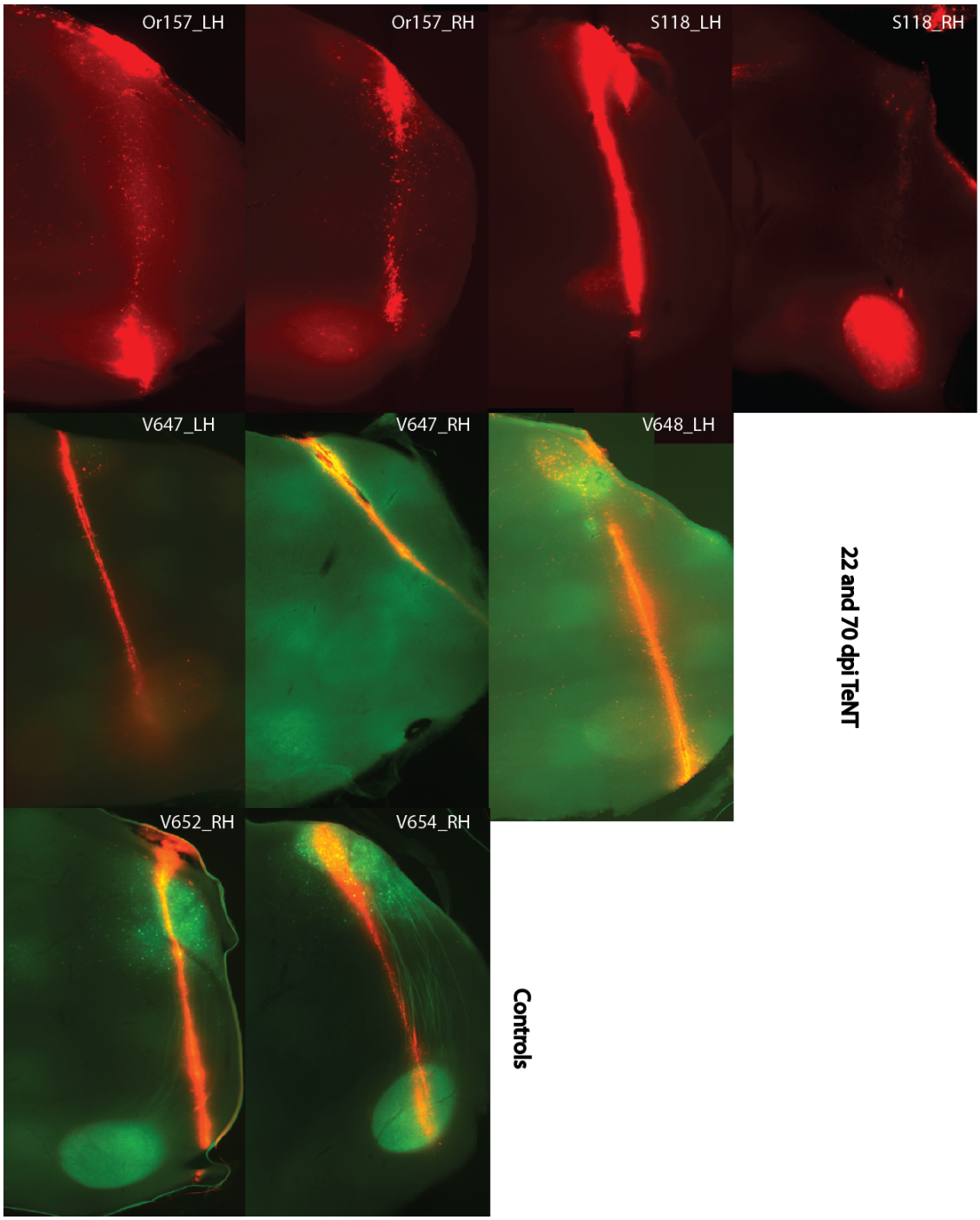

Supplementary Figure 15: *Histology to confirm the high-density silicone electrode location in the acute head-fixed animal recordings. The red trace represents the electrode location. The green trace represents the second electrode location in animals that were recorded twice, 40 days apart. The white labels represent the animal IDs. "LH" and "RH" stands for left and right hemisphere, respectively.*

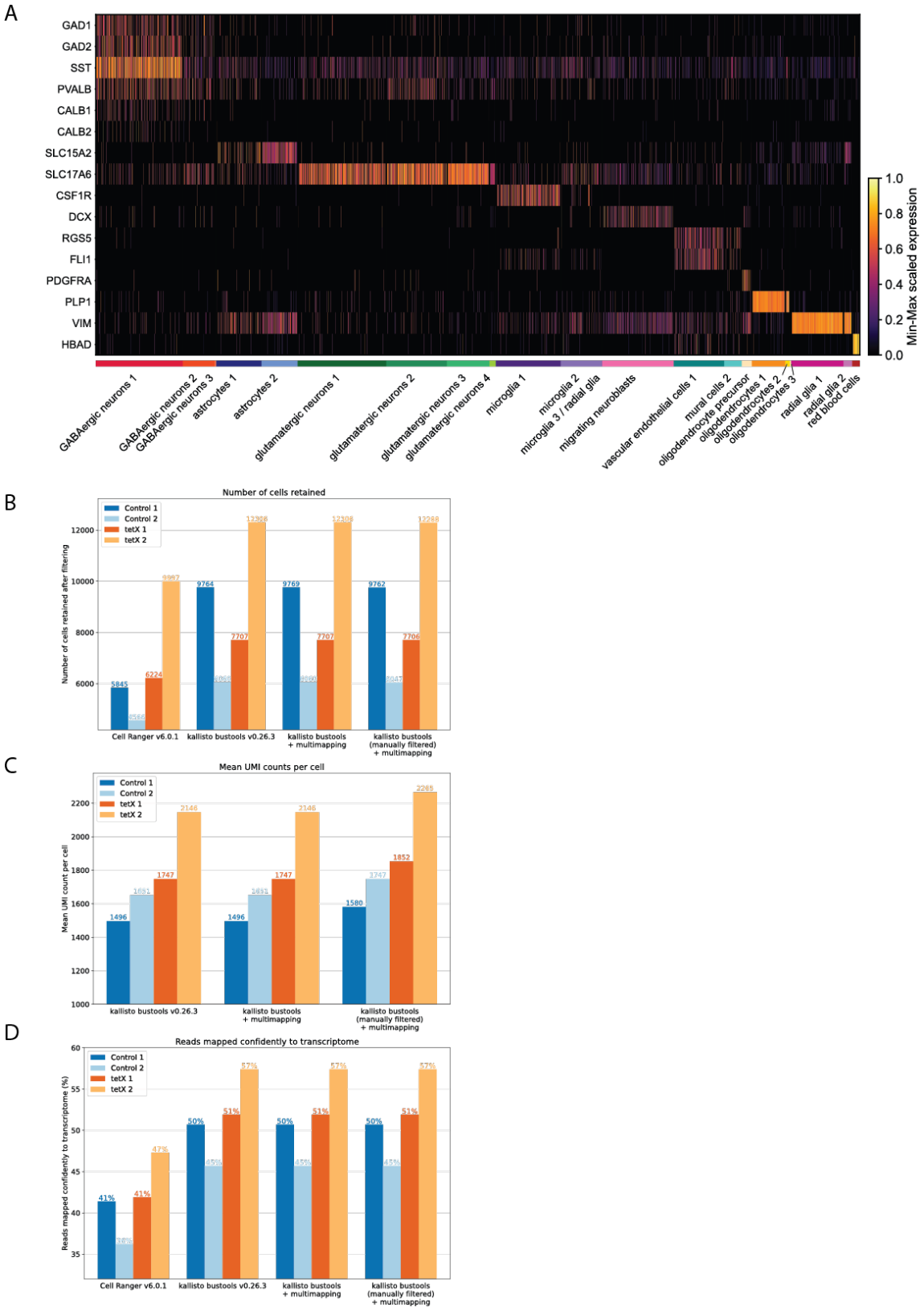

Figure legend on next page.

1103 ***Supplementary Figure 16:*** *Comparison of different pre-processing methods for the HVC single-cell RNA*
1104 *sequencing datasets and marker genes.* ***A*** *Heatmap showing min-max scaled expression of cell type marker*
1105 *genes for each cell type (data from both control and TeNT-treated animals).* ***B*** *Number of cells retained after*
1106 *quality control for each dataset and alignment method.* ***C*** *Mean UMI counts per cell for each dataset and pre-*
1107 *processing method.* ***D*** *Percentage of reads confidently mapped to transcriptome for each pre-processing*
1108 *method.*

A

Deflection durations (half-widths) in ms (mean ± SD)						
	3-5 DPI	15 DPI	30 DPI	45 DPI	60 DPI	75 DPI
Control animal 1 (OR295)	44.2083 ±16.0885	50.7321 ±21.5322	47.7079 ±16.4028	49.5889 ±18.5678	45.4170 ±15.4166	48.2883 ±18.5856
Control animal 2 (PK31)	43.9120 ±15.5607	46.5072 ±17.6237	36.7974 ±15.6453	42.4989 ±15.8985	37.8048 ±15.2497	35.3157 ±15.2297
TeNT-treated animal 1 (B138)	24.7074 ±11.0296	20.4568 ±5.7482	26.2938 ±10.4427	32.1460 ±13.1017	36.8212 ±15.3777	41.4122 ±15.9937
TeNT-treated animal 2 (OR296)	34.6744 ±10.7396	29.2852 ±8.3464	29.5713 ±9.5446	31.4171 ±11.5461	39.8151 ±10.5067	42.9507 ±14.0682

B

Deflection amplitudes in µV (mean ± SD)						
	3-5 DPI	15 DPI	30 DPI	45 DPI	60 DPI	75 DPI
Control animal 1 (OR295)	-136.3911 ±28.7491	-155.0317 ±49.3434	-151.5708 ±35.8116	-149.0358 ±34.9365	-152.4109 ±33.1907	-150.5303 ±33.8846
Control animal 2 (PK31)	-111.9867 ±20.8258	-117.1694 ±26.5227	-133.9981 ±26.5174	-130.6166 ±25.9310	-138.6591 ±26.7510	-135.2756 ±25.9969
TeNT-treated animal 1 (B138)	-538.6617 ±307.8410	-816.7580 ±371.9481	-705.8811 ±267.1738	-422.1097 ±143.1100	-306.8821 ±101.9335	-261.2531 ±80.5379
TeNT-treated animal 2 (OR296)	-174.6613 ±39.6156	-251.7470 ±70.1546	-337.3158 ±94.5369	-525.5973 ±157.8933	-228.3434 ±48.9163	-162.6949 ±35.6879

1109
1110 *Table legend on next page.*
1111

1112 ***Supplementary Table 1:*** *Amplitudes and durations of the chronic voltage deflections measured throughout the*
1113 *recording.* ***A*** *Mean duration (calculated as the distance from the onset to the half-width point of the event) in*
1114 *ms of voltage deflection events with standard deviation, each row represents an event from one control (Or*
1115 *295, PK31) or TeNT-treated (B138, Or296) animal. The data was sampled at 3-5, 15, 30, 45, 60, and 75 dpi.*
1116 ***B*** *Mean amplitudes (in µV) of voltage deflection events with standard deviation.*
1117
1118

Dataset (short name)	Species	Condition	Brain area	Replicate #	Technology	Pre-processing tool	# of cells retained after QC	Sequencing depth (number of reads processed)	Reads mapped confidently to transcriptome (%)	Mean UMI count per cell	Total UMI count
C1	Taeniopygia guttata	cag-neonGreen	HVC (both hemispheres)	1	10xv3	kallisto bustools	9,763	744,473,151	50.7	1580.8531	15,433,015
C2	Taeniopygia guttata	cag-neonGreen	HVC (both hemispheres)	2	10xv3	kallisto bustools	6,047	787,232,472	45.7	1747.639	10,568,132
E1	Taeniopygia guttata	dlx-TeNT-GFP	HVC (both hemispheres)	1	10xv3	kallisto bustools	7,706	867,768,600	51.9	1852.4215	14,274,784
E2	Taeniopygia guttata	dlx-TeNT-GFP	HVC (both hemispheres)	2	10xv3	kallisto bustools	12,288	810,253,355	57.4	2265.4258	27,837,586

1119 ***Supplementary Table 2:*** *Overview of single-cell RNA sequencing datasets.*
1120
1121